The star-disk interaction in Young Stellar Objects

Hernán Cerviño Asorey
Mestrado em Astronomia e Astrofísica
Departamento de Física e Astronomia
2021

Orientador
Prof. Dr. Jorge Filipe da Silva Gameiro, Faculdade de Ciências

U.PORTO

FACULDADE DE CIÊNCIAS
UNIVERSIDADE DO PORTO

Todas as correções determinadas pelo júri, e só essas, foram efetuadas.

O Presidente do Júri,

Porto, _____/_____/_____

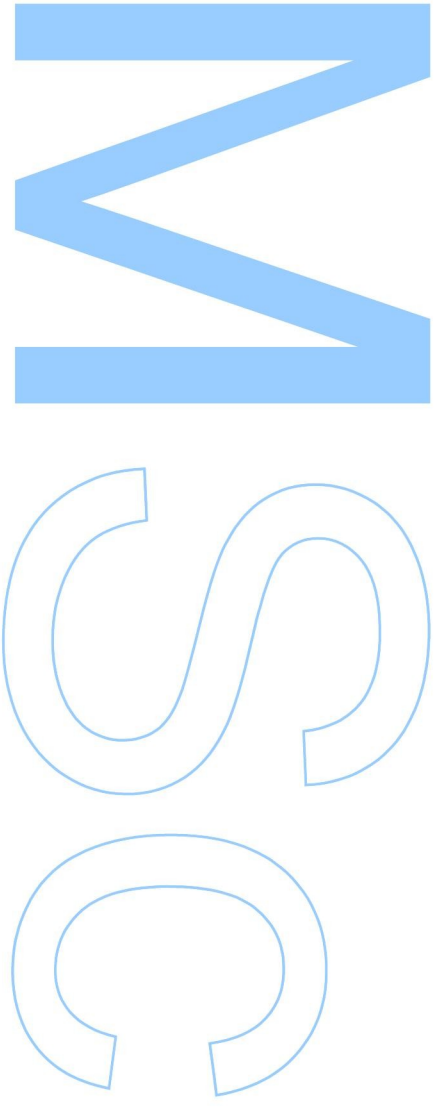

UNIVERSIDADE DO PORTO

MASTERS THESIS

The star-disk interaction in Young Stellar Objects

Author:
Hernán CERVIÑO ASOREY

Supervisor:
Jorge Filipe DA SILVA GAMEIRO

A thesis submitted in fulfilment of the requirements
for the degree of MSc. Astronomy and Astrphysics

at the

Faculdade de Ciências da Universidade do Porto
Departamento de Física e Astronomia

December 16, 2021

" Vivos refrexos,
Cintileando com'as estrelas,
Pintan mil cores no chan caendo,
E fan qu'a tola d'a fantesia,
Soñe milagres, finxa portentos. "

Rosalía de Castro, Galician poetess

Acknowledgements

At the first place and mainly, I would like to reveal my deep gratitude to my advisor Prof. Dr. Jorge Gameiro, whose support, help and knowledge were constant during the elaboration of this dissertation, highlighting his entire availability for any subject.

I also wish to thank all my teachers and colleagues who accompanied me during the Master's degree and contributed, in good measure, to this dissertation; specially those who became my Portuguese friends.

I would like to remember my old and exceptional friends who have always been an essential support and guidance.

Finally, an special word to my family and to Elena. Without them, this dissertation would be impossible and senseless.

UNIVERSIDADE DO PORTO

Abstract

Faculdade de Ciências da Universidade do Porto
Departamento de Física e Astronomia

MSc. Astronomy and Astrphysics

The star-disk interaction in Young Stellar Objects

by Hernán CERVIÑO ASOREY

Young Stellar Objects are stars on their earlier phase of evolution. This dissertation centres on a specific kind of Young Stellar Objects called Classical T Tauri stars. These stars are characterised by their low mass and the presence of a circumstellar disk created from the material which was part of the protostar which led to the Classical T Tauri star.

This kind of stars shows an appreciable star-disk interaction in the form of accretion of matter from the circumstellar disk to the star and outflows of matter out of the stellar object, such as stellar wind, jets, etc. These accretion and outflow processes present a high interest since it is relevant to understand how they work so as to comprehend how these star-disk systems evolve.

This dissertation addresses both theoretical and observational points of view. Regarding the theoretical perspective, we briefly introduce the formation of these Young Stellar Objects, focusing on Classical T Tauri stars, as well as the main notions related to accretion and outflow phenomena. From an observational perspective, we work with spectroscopic data from the Classical T Tauri star RY Tau, provided by the SPIRou spectrograph. We study the accretion and outflow processes by analysing the variability of several near-infrared spectral lines and two optical lines during some nights in September 2018.

UNIVERSIDADE DO PORTO

Resumo

Faculdade de Ciências da Universidade do Porto
Departamento de Física e Astronomia

Mestrado em Astronomia e Astrofísica

A interação estrela-disco em 'Young Stellar Objects'

por Hernán CERVIÑO ASOREY

Os 'Young Stellar Objects' são estrelas na sua fase inicial de evolução. Esta dissertação foca-se num tipo específico de 'Young Stellar Objects' chamado estrelas 'Classical T Tauri'. Estas estrelas caracterizam-se pela sua pequena massa e pela presença dum disco circum-estelar criado a partir do material que fazia parte da protoestrela que deu lugar à estrela 'Classical T Tauri'.

Este tipo de estrelas apresenta uma interação estrela-disco relevante em forma de acreção de matéria do disco circum-estelar para a estrela e em forma de 'outflows' de matéria para fora da estrela, tais como ventos estelares, jatos, etc. Estes processos de acreção e 'outflow' têm um grande interesse dado que é importante perceber como funcionam com o objectivo de compreender a maneira em que o sistema estrela-disco evolui e a perda de momento angular do sistema.

Esta dissertação aborda tanto do ponto de vista teórico como o observacional a evolução do sistema estrela/disco. Relativamente à perspectiva teórica, introduzimos brevemente a formação destes 'Young Stellar Objects', centrando-nos nas estrelas 'Classical T Tauri', bem como as principais noções relacionadas com fenómenos de acreção e 'outflow'. Na componente observacional, trabalhamos com dados espectroscópicos da estrela 'Classical T Tauri' chamada RY Tau, obtidos com o espectrógrafo SPIRou. Estudamos os processos de acreção e 'outflow' mediante a análise da variabilidade de algumas riscas espectrais do infravermelho próximo e duas riscas da banda do ótico obtidas em simultâneo com as observações no infravermelho.

Contents

List of Figures

Glossary

CFHT	Canada-France-Hawaii Telescope
CrAO	Crimean Astrophysical Observatory
CTTS	Classical T Tauri Star
FWHM	Full Width at Half Maximum
HR	Hertzsprung–Russell
IR	InfraRed
JD	Julian Date
MHD	MagnetoHydroDynamics
MJD	Modified Julian Date
MS	Main Sequence
NIR	Near-InfraRed
NRC	National Research Council
PCA	Principal Component Analysis
PMS	Pre Main Sequence
SED	Spectral Energy Distribution
SLS	SPIRou Legacy Survey
SPIRou	Spectropolarimètre Infrarouge
TTS	T Tauri Star
UV	UltraViolet
VALD	Vienna Atomic Line Database
WTTS	Weak T Tauri Star

YSO Young Stellar Object

Chapter 1

Introduction

From the very beginning of the humanity existence, every human group has asked itself many questions about what they were seeing up in the sky. 'Where do these bright points come from?', 'How were they formed?', 'Was our Sun formed in the same way?', 'And... What about our planet?'. All these questions sound familiar to every person interested about his or her surroundings. Inevitably, the answers to these questions are hidden in science, namely in the Stellar Formation branch of Astronomy. So as to understand the processes which respond to the previous issues, we need to have a look into a specific type of low-mass stars called T Tauri stars (TTSs). These objects are young stars, we allude to them as Young Stellar Objects (YSO), which define a current laboratory so as to study the stellar formation processes.

In this chapter, we briefly explain how low-mass stars are formed and introduce these T Tauri Stars, focusing on Classical T Tauri stars (CTTSs) subtype. We describe their main characteristics and mention the accretion and outflow processes related to them. To finish, we describe how this dissertation is structured.

1.1 Low-mass stars formation

Star formation is a well studied issue in Astronomy and Astrophysics. It is fundamental to understand the stellar formation process so as to give an answer to many questions beside the star formation itself. The origin of planetary systems like ours is related to the formation of the host star. Below, we concisely describe how a low-mass star is formed.

It is known that, in galaxies, there exist huge structures named molecular clouds mainly constituted by interstellar dust, gas and containing some dense cores, as we can

see in Figure 1.1 a. As a result of gravitational interaction inside these structures, some objects called protostars are formed in the denser areas (Stahler and Palla [2004]). At a first stage, these protostars are only visible in the infrared band, since they are surrounded by an opaque cloud of those materials which originated the protostar, as can be seen in Figure 1.1 b and c. After that, when the aforementioned cloud is dissipated, the star becomes visible in the optical band, Figure 1.1 d.

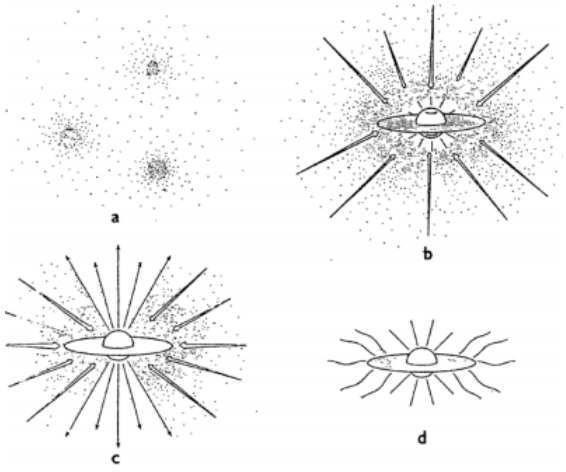

FIGURE 1.1: Star formation stages. From Shu et al. [1987].

These Pre Main Sequence (PMS) stars are completely convective. On their way to the Main Sequence (MS), they go through the Hayashi track (Hayashi [1961]) and the Henyey track (Henyey et al. [1955]).

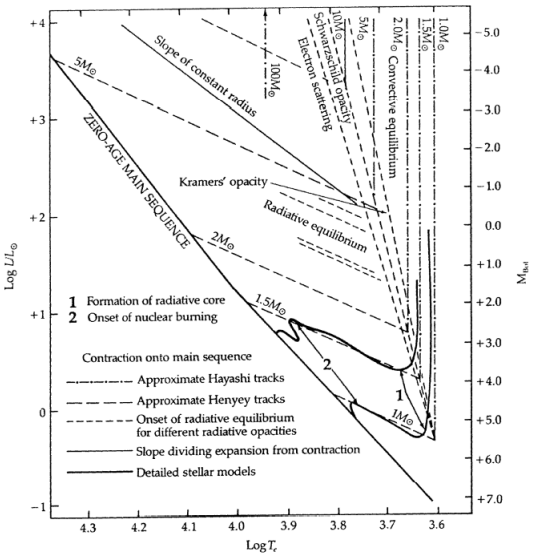

FIGURE 1.2: Hayashi and Henyey tracks for stars of different masses. From Collins [1989].

On the Hayashi track, the effective temperature of the star depends weakly on the stellar luminosity. Thus, since the stellar main source of energy is the gravitational one, the star contracts and its luminosity decreases but its effective temperature remains practically constant. Then, the stellar contraction originates the increase of the effective temperature of the star, while the luminosity increases smoothly, and the star stops being completely convective, forming a radiative core and getting in the Henyey track. This implies an increase of the magnetic field complexity (Monteiro [2019]). This last described track ends at the moment that the star enters the stable MS phase when the stellar core temperature reaches 10^7 K approximately and begins fusing hydrogen into helium. Once this takes place, the star has developed a fully radiative nucleus and a convective envelope, constituting a completely formed star in equilibrium, that is, a star whose thermal pressure counteracts the gravitational collapse.

1.2 An approach to Classical T Tauri stars

Once we have introduced a summary about star formation, we will focus on the particular type of stars being analysed in this work. There exists a specific kind of YSO called T Tauri stars. These bodies belong to the previously described PMS and are characterised by possessing a low mass, equal or less than 2 $M_\odot$, and age between 1 and 10 million years (de Albuquerque [2015]). In the Hertzsprung–Russell (HR) diagram, T Tauri stars are located at the right side of the MS, as shown in Figure 1.3, and with spectral class ranging from F to M type (de Albuquerque [2019]). T Tauri stars are classified in two types: Classical and Weak T Tauri stars.

From a spectroscopic point of view, there exist several differences between these two types of T Tauri stars. Figure 1.4 shows three spectra of CTTSs and one Weak T Tauri star (WTTS) spectrum. As can be seen, CTTSs show strong emission lines, specifically Balmer lines, neutral and ionised metals. The most characteristic emission line in these stars is Hα line, at $\lambda = 6563$ Å. The accretion disk or the interaction between accretion disk and the star is also responsible for the Balmer jump and the excess emission in the blue and ultra-violet (UV) bands. In contrast, WTTSs do not show strong emission lines as Figure 1.4 shows. These stars are more evolved than CTTSs and it is possible to appreciate the lack or dissipation of the accretion disk. All these facts show that CTTSs are more active than WTTSs. However, the big absorption lithium line at $\lambda = 6708$ Å is common to both

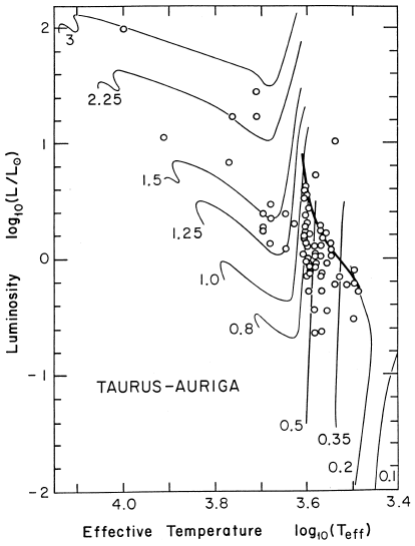

FIGURE 1.3: HR diagram for TTSs from Taurus-Auriga molecular cloud. The points represent the studied stars and the lines the stellar tracks for masses from 0.1 $M_\odot$ to 3 $M_\odot$. From Stahler [1988].

types of TTSs and is indicative of their youth as this element is one of the first to be burnt inside the star. As the star evolves, this line becomes fainter and smaller.

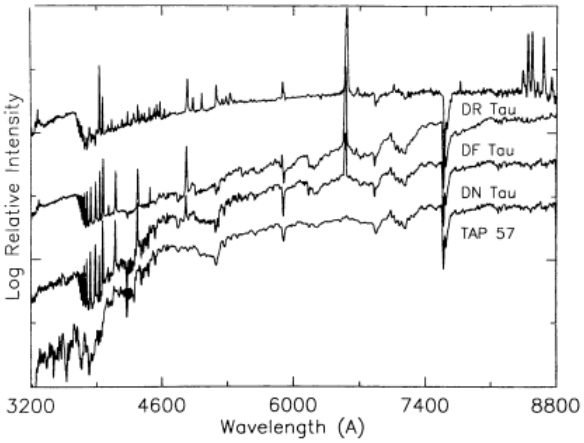

FIGURE 1.4: CTTS spectra (DR Tau, DF Tau and DN Tau) and WTTS spectrum (TAP 57). The compared spectra are normalised to the continuum and vertically shifted just for clarity. From Bertout [1989].

Another main difference between CTTSs and WTTSs stars is the presence of the ultra-violet and optical continuum excesses emission, also known as veiling of photospheric lines. As we can see in Figure 1.4, the photospheric lines in the CTTS appear less deep and weaker than in the WTTS. Thus, veiling has usually been assigned to non-photospheric

excess continuum emission and quantified as follows.

$$r_\lambda = \frac{F^\lambda_{\text{excess}}}{F^\lambda_{\text{phot}}} = \frac{F^\lambda_* - F^\lambda_{\text{phot}}}{F^\lambda_{\text{phot}}}, \tag{1.1}$$

where F^λ_* and F^λ_{phot} are respectively the T Tauri and underlying photospheric fluxes (generally taken as the flux of a normal star with the same spectral class of the T Tauri star).

Our interest focuses on CTTSs since they present a circumstellar accretion disk interacting with the host star. The host object gets mass from the disk, about $10^{-8}M_\odot/\text{yr}$, and loses mass too, around $10^{-9}M_\odot/\text{yr}$, (de Albuquerque [2015]). It is also known that this star-disk interaction should be related with the strong magnetic activity of the system.

Thus, the outflow and accretion activities can be addressed using spectroscopy. The study of the spectral lines is useful to understand the characteristics and dynamics of the circumstellar medium, in other words, the gas motion out from the star as stellar wind, meaning outflows, and towards the body, that is accretion. The outflow of matter is indicated by the presence of overlapped absorption on emission lines shifted to smaller wavelengths, named blueshifted absorption, which is called a P Cygni profile. Such outflows evidence is very common in Hα line. Furthermore, the presence of mass accretion is demonstrated by the existence of absorption shifted to bigger wavelengths, called redshifted absorption, known as an Inverse P Cygni profile. An instance of this last case is given by the He I line (Petrov [2003]). The P Cygni and Inverse P Cygni profiles are illustrated in Figure 1.5. There also exist other lines as [OI] or [SII] whose emission is related to outflow processes but which do not present any P Cygni profile. These are called forbidden lines and are caused from rarefied gas flows at considerable distance from the star.

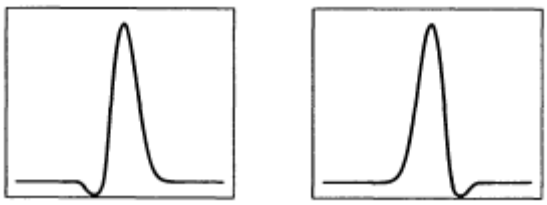

FIGURE 1.5: P Cygni (left) and Inverse P Cygni (right) profiles. From Reipurth et al. [1996].

The spectroscopic indications of the outflow and accretion processes derive from distinct regions of the star-disk system, which are characterised by different densities and temperatures. As it is schematized in Figure 1.6, most of the broad emission lines are emitted on the accretion flows, though a few narrow emission lines are thought to be created in the accretion shock region, near the stellar surface. This magnetospheric accretion process describes how material from the circumstellar disk is transported towards the inner part of the disk (0.1 AU approximately) and, as a consequence of the high temperature caused by the radiation field of the host star, the transported material begins to sublimate creating the near-infrared (NIR) excess. Besides, the disk is truncated by the stellar magnetosphere at few stellar radii and the material is accreted by the host star following the magnetic field lines, originating the broad emission lines. The narrow lines and X-rays are caused by the shock between the infalling gas, at free-fall velocities, and the stellar photosphere.

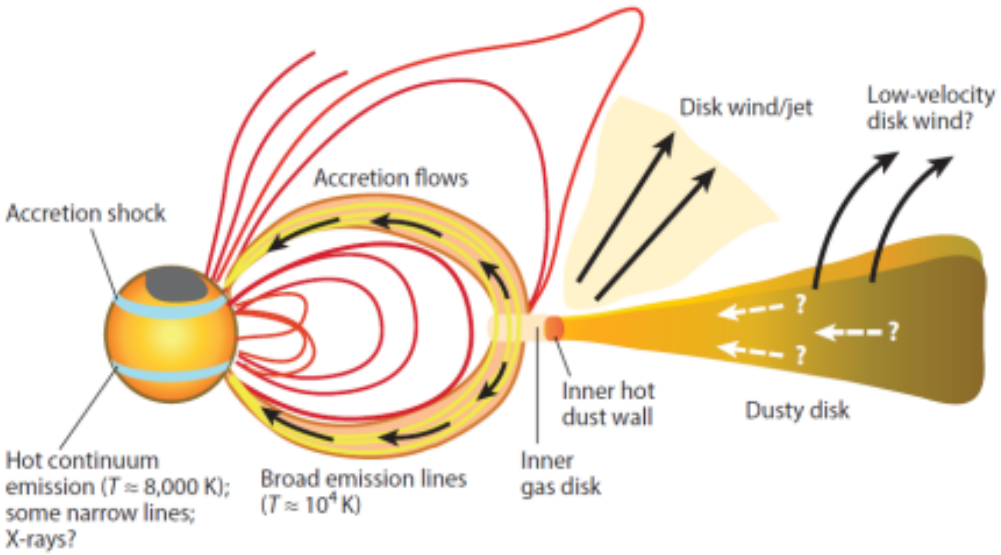

FIGURE 1.6: Magnetospheric accretion and stellar and disk outflows in a CTTS. From Hartmann et al. [2016].

Regarding the accretion disk around these stars, its formation is due to the rotating molecular cloud contraction which originates a protostar plus a Keplerian disk as a result of the angular momentum conservation. Since the interstellar medium is constituted by 99% gas and 1% dust, the composition of an accretion disk on its initial stage shall be the same (Ercolano and Pascucci [2017], Williams and Cieza [2011]). The size of these disks is thought to be between 20 AU and 200 AU (Williams and Cieza [2011]), despite being difficult such estimate, since the emission of the cold external part is arduous to detect.

Regarding the typical lifetime, it is thought to be from 3 Myr to 5 Myr approximately, although few systems have been reported with ages varying from less than 1 Myr to 10 Myr (Ercolano and Pascucci [2017], Gallet and Bouvier [2013], Gorti et al. [2016], Hernández et al. [2008], Williams and Cieza [2011]).

A more technical classification of YSO has been done by taking into account the infrared (IR) excess observed in these bodies. Thus, the IR spectral index is defined by

$$\alpha_{\mathrm{IR}} = \frac{\mathrm{d}\log \lambda \mathrm{F}_\lambda}{\mathrm{d}\log \lambda}, \tag{1.2}$$

where λ represents the wavelength and $\lambda \mathrm{F}_\lambda$ is the flux measured per logarithmic wavelength interval (usually between 2.2 μm and 10 μm) or flux density. Now, it is possible to classify these PMS objects as a function of the value of the infrared spectral index (Lada and Wilking [1984], Adams et al. [1987], Stahler and Palla [2004]):

- Class 0: they are the most deeply embedded sources, essentially low mass protostars. No optical or NIR emission, only visible at far-infrared and millimetre bands. They were characterised after the other three classes (Barsony [1994]).
- Class I: $\alpha_{\mathrm{IR}} > 0$, the YSO is inside a dense core and it is still optically hidden.
- Class II: $-1.5 < \alpha_{\mathrm{IR}} < 0$, the YSO is less embedded and normally surrounded by a circumstellar disk. They typically correspond to CTTSs.
- Class III: $\alpha_{\mathrm{IR}} < -1.5$, brighter YSO whose accretion disk has disappeared, mostly at least. They typically correspond to WTTSs.

Figure 1.7 shows these four different classes.

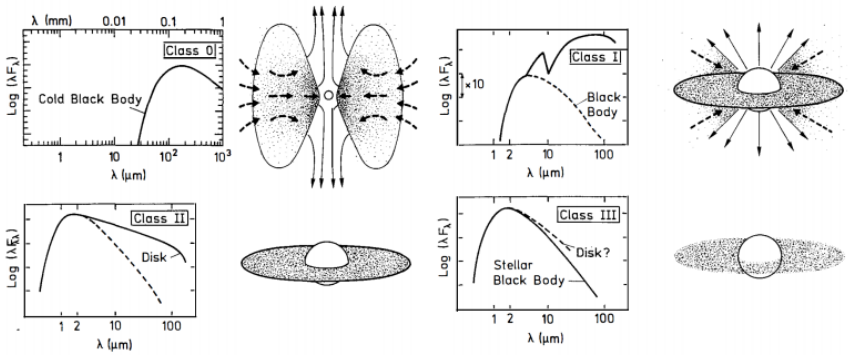

FIGURE 1.7: Class 0, I, II and III of YSO according to the infrared spectral index value. Spectral Energy Distribution (SED) and illustration. Adapted from André [1994].

1.3 Dissertation structure

After this brief introduction, in Chapter 2, we discuss the main theoretical issues of the star-disk interaction and how this process affects the outflow and accretion phenomena. Then, in Chapter 3, we present the SPIRou Legacy Survey (SLS), the data reduction and preliminary analysis done to the SPIRou data. We also introduce the main characteristics of our goal star RY Tau. In Chapter 4, we address the treatment of the SPIRou spectroscopic data of RY Tau and the analysis of the main emission lines shape and behaviour during the nights of observation. This helps us to understand how accretion and outflow phenomena occur between this star and its circumstellar disk. Furthermore, we study the equivalent width values and their evolution for all these emission lines, which allow us to extract some judgements about the variability of accretion and outflow processes during the observation nights. We also address a quantification of the absorption component of the emission lines so as to compare the absorption between different lines as well as to study the dynamics of the star-disk system. Lastly, in Chapter 5, we include the main conclusions of this work.

Chapter 2

Star-disk interaction and its relation with accretion and outflows

The star-disk interaction in TTSs can be described as an equilibrium between the accretion and outflow phenomena. Some authors (Hartigan et al. [1995], Cabrit [2007]) have carried out some research and concluded that accretion is the main effect in this dual process. The outflow seems to be directly related to the accretion process (when one of them is considerable, so is the other), but as a consequence of the mass accretion.

The study of these mechanisms turns out to be really relevant so as to understand the stellar evolution and the planet formations process.

2.1 Accretion

Historically, there exist several models which have tried to explain how accretion works. Maybe, the most relevant are the classic models by Shakura and Sunyaev (Shakura and Sunyaev [1973]) or Linden-Bell and Pringle (Lynden-Bell and Pringle [1974]) and the magnetospheric models. The classic model holds that the accretion disk extends to the stellar surface, with the formation of a boundary layer (inmost part of the disk) which emits a strong UV radiation. Afterwards, this vision was proved not to be correct due to the existence of strong stellar magnetic fields which disrupt the disk at few stellar radii of distance from the surface of the host star.

In order to understand properly the accretion mechanism, we need to summarise how the accretion disk behaves according to the standard model. In the case we can assume that the mass of the host star is much larger than the mass of the disk, the disk rotation is

Keplerian and so the mass of the disk has a differential rotation. The temperature of the disk increases as the distance to the star diminishes (at 10 AU, it is 100 K approximately) and there exist radiation emission since the energy originated by rotation is converted into thermal energy, due to viscosity (Petrov [2003]). At the same time, the lost of energy caused by viscosity (disk emission), makes matter to move inward to inferior orbits and finally, to get accreted.

Accretion disks are usually categorised into active or passive, depending on the disk luminosity. Active disks are those which present an own luminosity and passive disks are characterised by re-radiating absorbed starlight in the IR (de Albuquerque [2015]). As normal for active disks, the star-disk system luminosity is higher than the star's, while for passive disks, the luminosity of the star-disk system is similar to the star's.

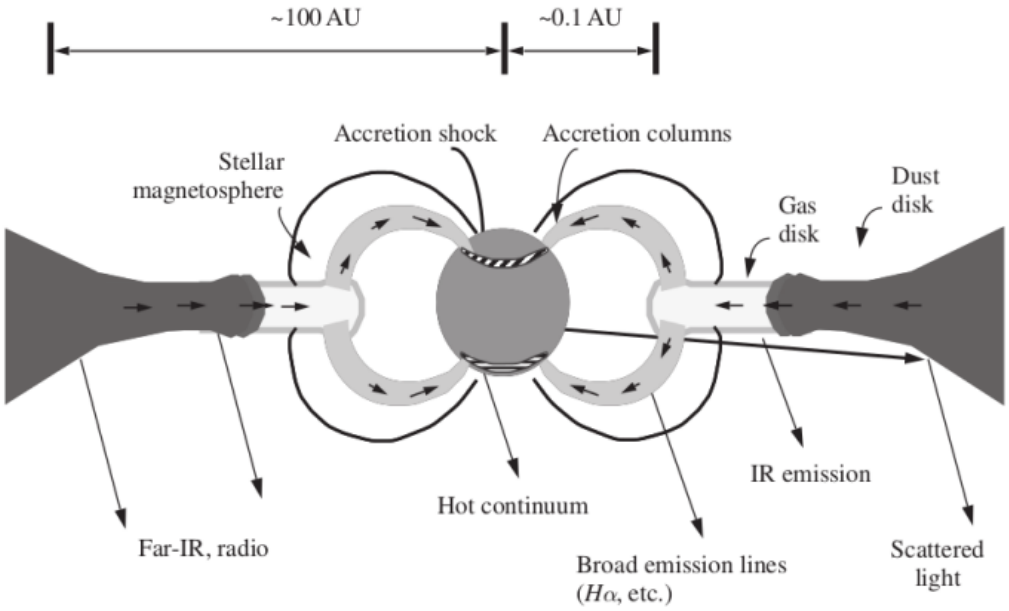

FIGURE 2.1: Accretion process in TTSs. Adapted from Stahler and Palla [2004].

The standard model presented some defects that push to the search of other models. Some facts that the standard model could not explain were related to the broadening and intensity of some emission lines which were too strong to be produced by a boundary layer. The standard model also does not explain the high variability of emission lines as well as the asymmetry in line profiles. Figure 2.1 illustrates the magnetospheric or MHD model for TTSs, where it is possible to see the accretion disk enclosing the host star and the accretion of matter from the disk into the star. The MHD model became important when strong magnetic fields were observed in CTTSs (Basri et al. [1992]). In such case, the

magnetic field truncates the inner part of the disk since the magnetic pressure is higher than the gas pressure. As the matter is ionised at the inner part of the disk, it will follow the field lines. Figure 2.1 also indicates the different emission lines from each source: far-IR and radio from the external disk, IR from the inner disk and the broad emission lines such as Hα from the infall area. This emission depends on the temperature and density of the medium. Such wide lines are a consequence of high velocities and, thus, accretion and outflow phenomena. It is important to note the scale variation, shown on the top of the illustration, that is, the inner part of the disk is shown at the same size that the remaining part, whereas their dimensions are completely different. In reality, it is not possible to observe this inner part of the disk as well as the connection between it and the host star, since we do not have instruments with sufficient spacial resolution nowadays.

This model is, up to now, the one which can explain best the strong emission lines observed in the spectra of CTTSs, thought to be consequence of material moving at high velocities, or the presence of non-axisymmetric spots on the surface of these stars, when accretion occurs only in some specific magnetic field lines or there is a misalignment between the stellar rotation axis and the magnetic field dipole.

Lastly, it is known that the emission lines in the CTTSs spectra can be used to detect accretion and characterise the magnetic stellar topology. Besides, accretion can also be measured in several ways. One of these methods is based on accretion luminosity which is given by

$$L_{\rm acc} = \frac{GM_{\rm s}\dot{M}_{\rm acc}}{R_{\rm s}}\left(1 - \frac{R_{\rm s}}{R_{\rm m}}\right), \tag{2.1}$$

where G is the gravitational constant, $M_{\rm s}$ is the stellar mass, $\dot{M}_{\rm acc}$ is the mass accretion rate, $R_{\rm s}$ is the stellar radius and $R_{\rm m}$ is the radius at which the disk is disrupted by the magnetic field (Manara [2014]). Accretion luminosity can be derived from different ways such as from veiling measurements, from the Balmer and Paschen continuum excesses or UV Balmer jump measurements (de Albuquerque [2019]).

Then, the mass accretion rate can be derived from Equation 2.1. Since $R_{\rm m}$ is dependent on the mass accretion rate and the magnetic field strength (Bouvier et al. [2006]), from observations, $R_{\rm m}$ is estimated to be in the range [$3R_{\rm s}$,$10R_{\rm s}$]. So, assuming $R_{\rm m}$=$5R_{\rm s}$, we have

$$1 - \frac{R_{\rm s}}{R_{\rm m}} \simeq 0.8, \tag{2.2}$$

obtaining

$$\dot{M}_{\rm acc} \simeq \frac{L_{\rm acc} R_{\rm s}}{0.8 G M_{\rm s}}. \tag{2.3}$$

This mass accretion rate is very dependent on the determination of $L_{\rm acc}$ and has a decrease with time allowing the determination of the disks evolution timescale (Hartmann [2008]).

2.2 Outflows

Outflow processes can be thought as the opposed phenomena to accretion and they appear in several ways. These outflow processes are also thought to be responsible for the lost of angular momentum, leading to the deceleration of the rotation of the host star, in addition to other magnetic mechanisms which also contribute to the previously mentioned spin-down. Normally, outflows are presented as collimated jets or uncollimated winds in both faces of the circumstellar disk and are oriented in opposite directions, as shown in Figure 2.2.

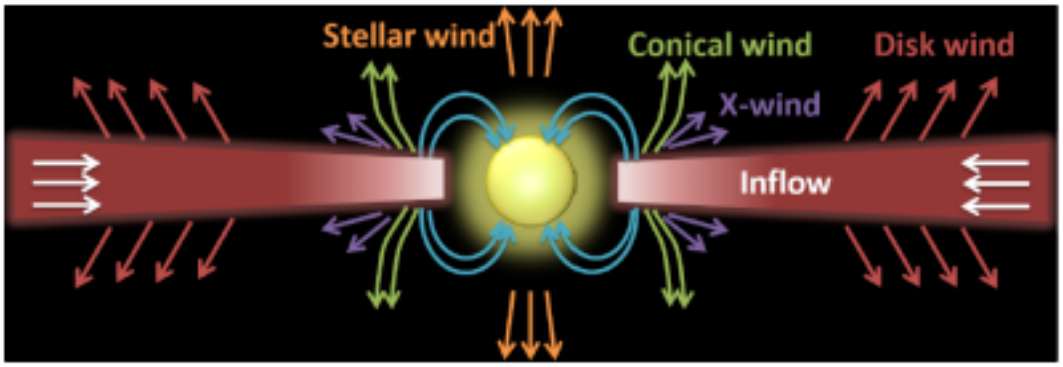

FIGURE 2.2: Outflow processes. From Romanova and Owocki [2015].

Namely, stellar winds are an outflow phenomenon which can be detected as superposed blueshifted absorptions in some emission lines as Hα and Ca II. This absorption is due to the presence of matter (wind opacity) which absorbs the radiation coming from the hottest source, that is, the star. Besides, when the flow is an extended beam of ionised matter along the stellar rotation axis, we refer to a jet. They can be detected by Hα, [NII], [OII] or [SII] emission lines (Petrov [2003]). Now, we shall carry out a revision through the main outflow shapes.

2.2.1 Stellar winds

As said before, stellar winds are thought to contribute to the stellar rotation deceleration since they present a considerably relevance related to angular momentum extraction.

Matt and Pudritz [2005] introduced an interesting model which holds that the outflow process could be sustained by a part of the energy released by accretion mechanisms. They concluded that, so as to interrupt the rotation acceleration of the star, it is enough for the mass loss rate of the star to be at 10% of the accretion rate. Lately, they also suggested that this mass loss rate cannot be superior to the 60% of the accretion rate. Otherwise, the accretion processes would be impossible since it would not overcome the outflow wind boost.

2.2.2 Disk winds, X-winds and conical winds

Some authors as Cabrit [2007] or Ferreira [2013] hold that the named disk winds could produce the deceleration of the disk rotation but they do not influence the stellar spin-down.

Additionally, other kinds of winds seem to be more relevant regarding this stellar rotation slowing down. These winds appear as a result of the interaction between the magnetic field of the star and the disk. There exists a X-region which splits two areas at a co-rotation radius R_X. The disk matter situated further from R_X, rotates at super-Keplerian velocities, which allows that part of this matter can escape from the disk as a wind. Besides, the disk material situated in the inner part of the disk rotates at sub-Keplerian velocities making accretion easier. Finally, at R_X, the Keplerian velocity and the stellar angular velocity are equal. The angular momentum transfer regulates the stellar rotation acceleration, since the angular momentum is carried from the accretion flow region to the inner part of the disk and, further from R_X, the so-called X-wind carries the angular momentum to the interstellar medium. Figure 2.3 illustrates the previous explanation.

Finally, conical winds have been studied by Romanova et al. [2009] as outflow processes which are propelled by magnetic pressure. Typically, they present the shape of a cone, their half-opening angle is between 30º and 40º and their composition up to 0.3 AU from the star consists of a 10% to 30% of the inner disk material. Among the main differences between these and the X-winds are that, for the conical winds, the truncation radius of the disk can be smaller than the co-rotation radius R_X, whereas for X-winds both radii

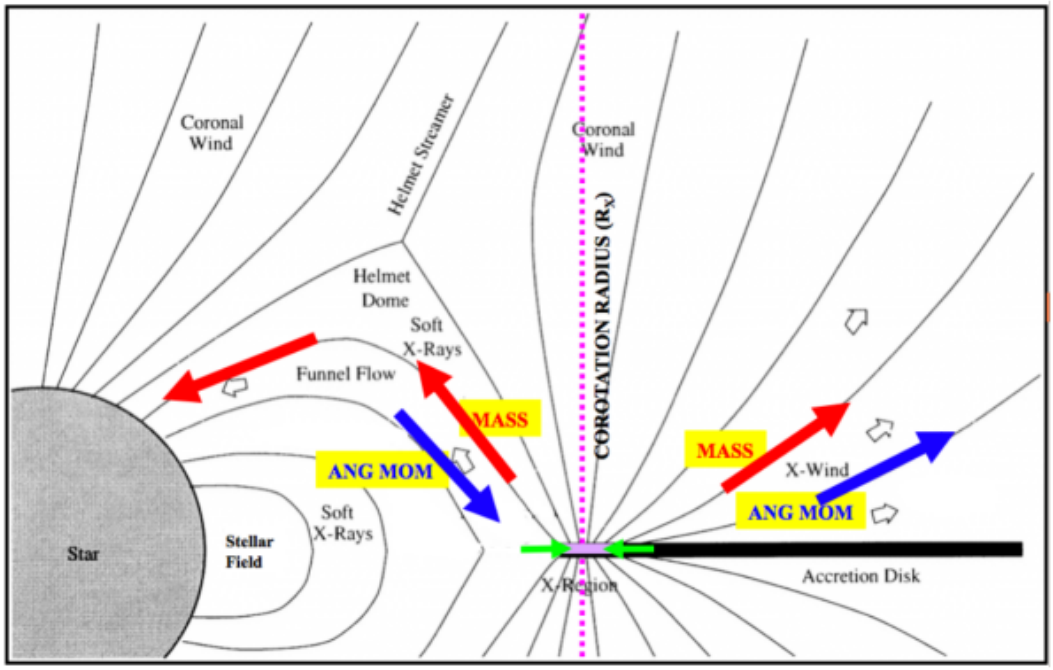

FIGURE 2.3: X-wind model illustration. From Bouvier et al. [2014].

coincide. Besides, the driven forces associated to these winds are different: conical winds are conducted by the magnetic pressure and X-winds by the centrifugal force.

2.2.3 Magnetospheric ejections

Magnetospheric ejections produce mass, energy and angular momentum interchange between the host star and the disk. This exchange occurs after an inflation process followed by a disconnection and a reconnection of the closed magnetospheric field lines between the star and the disk. Figure 2.4 shows this mechanism.

The expansion of the magnetic field lines is caused by a different angular velocity between the support points of the accretion columns, in other words, the differential star-disk rotation. In the disconnection phase, the material is ejected to the interstellar medium as magnetised plasmoids. After, during the reconnection phase, the inner magnetic structures close, completing a full cycle (Zanni and Ferreira [2012]). These authors also concluded that magnetospheric ejections are partially responsible for the rotation velocity of the star since they can remove angular momentum from the inner part of the accretion disk and also from the star if the ejected material rotates slower than the star itself. The disk-locking process in CTTSs is also well-explained by these outflow mechanisms. Disk-

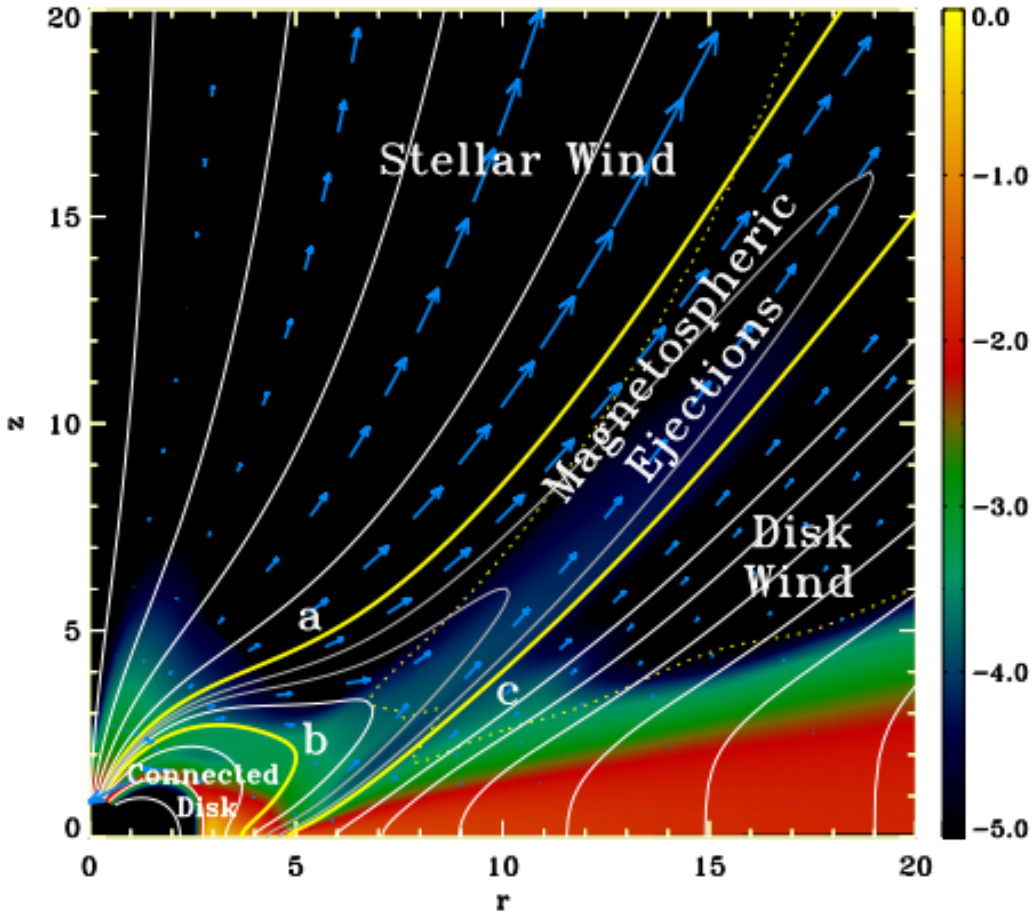

FIGURE 2.4: Magnetic ejections simulation. The white solid lines represent the sampled magnetic field lines and the yellow lines represent the boundaries (a, b and c) between the different outflow mechanisms which are illustrated: stellar wind, magnetospheric ejections and disk wind. From Zanni and Ferreira [2012].

locking process (Ghosh and Lamb [1979]) could be a possible explanation to the deceleration of the stellar rotation in YSOs, when both star and disk are trapped by the magnetic field, the star undergoes a spin-down. Nevertheless, the relevance of this phenomenon is being called into question by some recent research (Romanova et al. [2011]).

2.2.4 Jets

Jets are an outflow mechanism which consists of a considerably collimated structure where it is possible to distinguish several bright nodes as a consequence of the pulsed acceleration of their matter. Figure 2.5 shows this outflow mechanism. On the left panel, we can see the structure from a disk scale, the most remarkable characteristic is the spiral

or rotating nature of these jets. On the right panel, we can observe the jets from an envelope scale point of view, it is possible to see a very characteristic structure (spur shock) as well as a bright front (bow shock) created where the jet hits the interstellar medium. These structures are perpendicular to the disk and they are relatively easy to detect by low excitation forbidden lines.

Jets are thought to be a consequence of the interaction between the accreted matter and the star-disk system magnetic field (Frank et al. [2014]). Some of their main characteristics have also been studied. For CTTSs, the mass outflow rate fluctuates between 10^{-9} $M_\odot$/yr and 10^{-7} $M_\odot$/yr (Frank et al. [2014]), their sizes oscillate between 100 AU and 500 AU and their average velocity is about 170 km s^{-1} (Beckwith et al. [1996]).

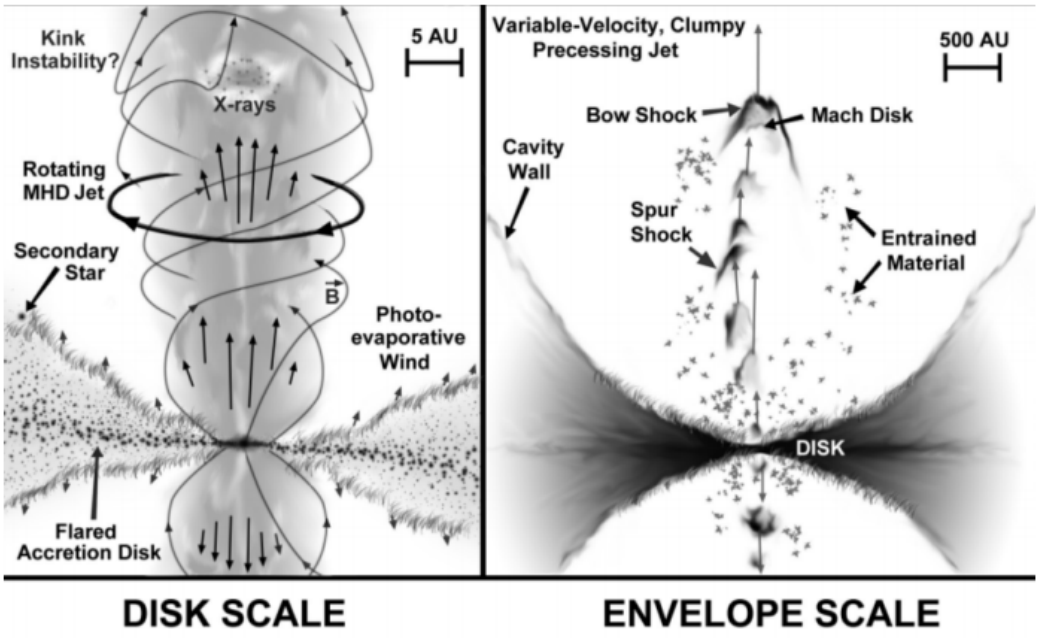

FIGURE 2.5: Jet structures in TTSs in two distinct scales. From Frank et al. [2014].

Chapter 3

The SPIRou Legacy Survey and RY Tau star

The aim of our specific work is to get a better understanding of the star-disk interaction of the CTTS RY Tau. Namely, the outflow phenomena can give us information about the disk wind and its evolution by analysing the variability of some particular emission lines. Besides, the mass accretion rate variation shall also help us to characterise the connection between accretion and outflow processes. To do this, we used SPIRou data obtained over several nights in September 2018.

In this chapter, we shall start by describing the SPIRou Legacy Survey and its main characteristics and objectives. Then, we will continue by addressing the necessary reduction for the SPIRou data and, finally, we will focus on describing our goal star RY Tau.

3.1 SPIRou Legacy Survey

SPIRou is a near-infrared spectropolarimeter and high-precision velocimeter operating in the Canada-France-Hawaii telescope (CFHT) on Maunakea, which is being used to detect exoplanets around low-mass stars as well as to detect and characterise the magnetic field of YSOs (Moutou et al. [2015]). Thanks to the featuring of a special optical material, SPIRou could improve transmission at wavelengths larger than $\lambda = 20\,000$ Å, which allowed the inclusion of the K band in the observations. This is a remarkable characteristic among most near-infrared velocimeters and makes SPIRou an optimal instrument so as to search exoplanets and to study stellar activity (Cloutier et al. [2017]). Namely, SPIRou

covers Y, J, H and K bands from the NIR, that is, from $\lambda = 9800$ Å to $\lambda = 23\,500$ Å (Moutou et al. [2015]).

Since the observation time needed to accomplish the goals of SPIRou is quite large, SPIRou is only understandable together with the SPIRou Legacy Survey which was thought to prolong for 300 nights during 3 years, at least, although this has not been accomplished due to some technical problems. This survey presents three main goals, which are to search some tens of exoplanets with specific characteristics in the neighbourhood of the Solar System; to describe the inner structure of several telluric or Earth-like planets and to investigate the influence of magnetic fields in the star and planet by studying these magnetic fields in YSOs (Moutou et al. [2015]).

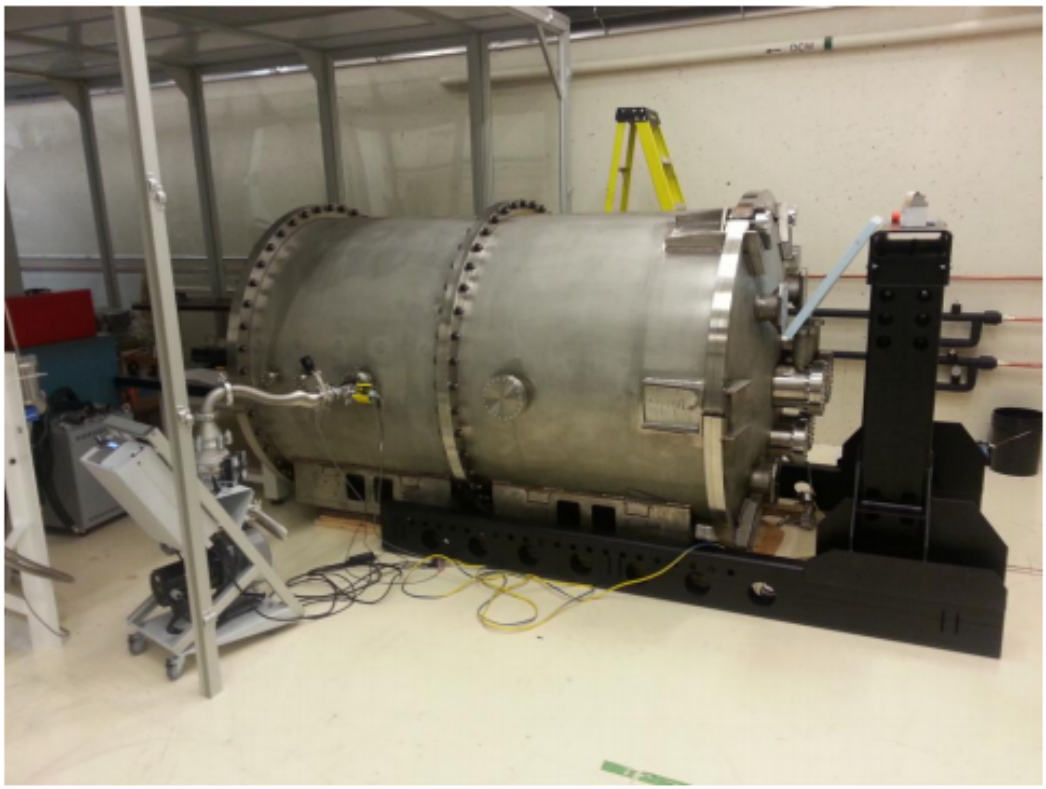

FIGURE 3.1: SPIRou cryostat at the National Research Council (NRC) Herzberg Astronomy and Astrophysics Research Centre. A cryostat is a device which keeps low cryogenic temperatures. From Moutou et al. [2015]

For our work, the SLS primary aim is the study of the magnetic field in YSOs together with its impact on the star-planet formation. Namely, CTTSs have been quite studied in the optical band due to their relative accessibility because of the existence of optical instruments. Naturally, enlarging this study to the near-infrared band is the most understandable path to follow. Typically, these YSOs are brighter in the near-infrared band and,

thus, observations of the SLS shall permit to survey bigger samples of stars (Moutou et al. [2015]).

Specifically, the SLS was thought to permit the spectropolarimetric monitoring of 40 CTTSs, as well as 20 class-I protostars and 80 WTTSs, from the Taurus/Auriga, TW Hya Association and ρ Ophiuchius stars forming regions, during 125 nights approximately. For CTTSs, this survey increased the sample and allowed a much better diagnostic about the magnetic field variation with stellar parameters. The survey also permitted the study of the inner regions of circumstellar disks surrounding CTTSs based on the characteristic signatures which are originated by these accretion disks (Moutou et al. [2015]).

3.2 SPIRou spectra reduction

As it was indicated in the previous section, SPIRou obtains a single-shot spectral domain from $\lambda = 9800$ Å to $\lambda = 23\,500$ Å, including Y, J, H and K bands. It presents a spectral resolution between 70 K to 75 K and supplies enough linear and circular polarimetric capacity so as to observe the stellar magnetic fields and dissect the stellar activity. It also obtains a signal-to-noise ratio of 100 per 2 km s^{-1} pixel for fainter stars, those with a magnitude of J=12 or K=11, allowing the study of a large amount of stars.

The spectra provided by SPIRou is divided in 49 orders. The first order begins at $\lambda \sim 9557$ Å and the last order ends at $\lambda \sim 25\,157$ Å, allowing the observation of the NIR spectrum spread over 15 000 Å.

Before the treatment and analysis of the data provided by SPIRou, it is necessary to conduct a reduction. The images were treated in the observatory by the installed pipeline, which uses the PCA-based correction technique Moutou et al. [2020]. These observations were performed without the polarimetry mode and so it is not possible to carry on a polarimetric analysis.

Furthermore, it is necessary to perform a reduction by correcting the telluric lines, which appear because of the called telluric contamination. Some molecules in our planet atmosphere absorb and emit light originating these lines which contaminate the object's spectrum. Furthermore, the absorption originated by the Earth's atmosphere is even more limiting for NIR spectroscopy. There exist several methods so as to remove these telluric lines, such as synthetic transmission methods or the telluric standard star method (Ulmer-Moll [2020]). In our case, the SPIRou postdoctoral fellow Andrés Carmona, provided the reduced spectra which will be introduced and explained later on. In Figure 3.2, we show

an example of this treatment for the order 9 of SPIRou spectrum corresponding to the He I ($\lambda = 10\,829.09$ Å) line. In the panel 3.2I, the narrow features correspond to the telluric lines, and panel 3.2II show the final spectrum after the telluric correction.

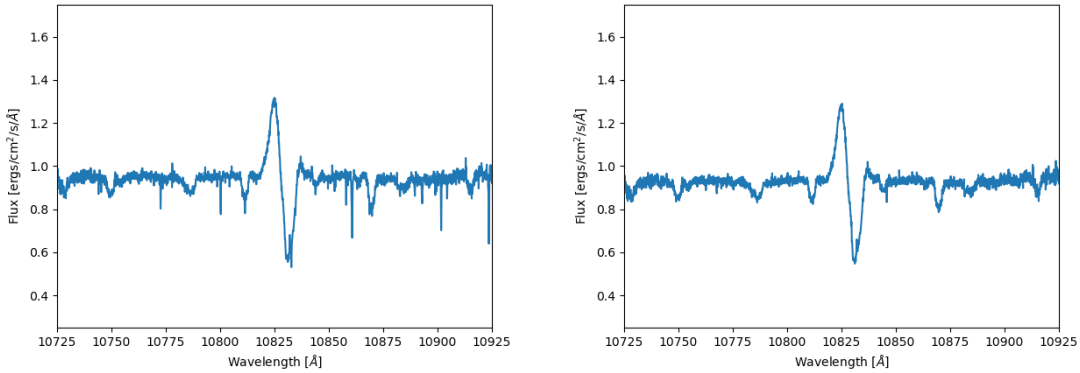

(I) Spectrum before the telluric correction.

(II) Spectrum after the telluric correction.

FIGURE 3.2: Section of the 9th order of a spectrum obtained by SPIRou, corresponding to the He I ($\lambda = 10\,829.09$ Å) emission line.

3.3 The T Tauri star RY Tau

RY Tau is the object of our practical study in this work. Before introducing the analysis and results derived from the SPIRou data, we shall present the main characteristics of this YSO. In Figure 3.3, we can observe a coloured image of RY Tau. This source is associated to an extended nebulosity and a remnant envelope close to the star (Takami et al. [2013]).

RY Tau was firstly observed in 1907 (Pickering [1907]) and it is a recognised Classical T Tauri Star which belongs to the Taurus-Auriga molecular cloud at a distance of approximately 150 pc. Several studies of this object have proved that it shows irregular photometric and spectroscopic variability in visible and NIR wavelengths. This variability is thought to be originated by different physical processes, such as the obscuration of the star caused by the circumstellar disk at high inclination and the stellar environment (Eiroa et al. [2002]), starspots and irregular accretion (Petrov et al. [1999]). A short summary of RY Tau characteristics and references are presented in Table 3.1.

It is obvious that each star-disk system presents a specific inclination in the line of sight of the observer. For instance, if the inclination is close to 0°, we see the system pole-on oriented but, if inclination is close to 90°, we see the system edge-on oriented. In our case, RY Tau belongs to an edge-on oriented system since its inclination was estimated as less than or approximately equal to 70° by Schegerer et al. [2008] and afterwards it was

FIGURE 3.3: Colour image of the RY Tau neighbourhood, performed from the long exposures in the four Sloan filters. RY Tau is the more vivid object, situated below the centre of the image and slightly to the right, still embedded in the nebula. From St-Onge and Bastien [2008].

estimated as $65.0^{+0.1}_{-0.1}$ by Long et al. [2019]. Such high inclination allows a better study of the accretion and outflow processes, since the observer's line of sight intersects the winds from the disk, making possible the analysis of these accretion and outflow phenomena as well as their interaction with the star and its circumstellar medium.

RY Tau has a long photometric data records, with extended series of photometric observations since the sixties until now, confirming its strong photometric variability. For instance, it has been reported a variation between 9.5 and 11.5 magnitudes in the V-band with a remarkable brightening between 1983-1984 and 1996-997 (Herbst and Stine [1984], Herbst et al. [1994], Zajtseva et al. [1996]). Furthermore, Zajtseva [2010] observed quasi-periodic variations of brightness during about 35 years (1965-2000), which were attributed to eclipses originated by dust clouds from the accretion disk. As a consequence of the photometric variability and the insignificance of the veiling, which is very weak and

Parameter	Value	Reference
RA (J2000.0)	04h 21m 57.4s	[3]
DEC (J2000.0)	$+28^\circ\ 26'\ 36''$	[3]
Effective temperature	5945 ± 142.5 K	[2]
$\log g$	3.8	[1]
Distance	150 ± 10 pc	[2]
Stellar luminosity	$13.5 \pm 1.7\ L_\odot$	[2]
Stellar radius	$3.3 \pm 0.25\ R_\odot$	[2]
Stellar mass	$2.08 \pm 0.1\ M_\odot$	[2]
Age	$4.7^{+1}_{-0.8}$ Myr	[2]

TABLE 3.1: RY Tau main parameters. [1] from Davies et al. [2020], [2] from Petrov et al. [2019] and [3] from Schegerer et al. [2008].

not variable, we can conclude that the photometric variability is related to dust extinction (Petrov et al. [2019]). However no stable period has been derived from photometric and/or spectroscopic monitoring. A quasi-stable period of 21.6 days has been measured recently (Petrov, private communication), larger than the expected 3 days period derived if we take in account the stellar parameters and system inclination. It has been difficult to identify the RY Tau spectral type and effective temperature since this star presents a high projected rotational velocity of 50 km s^{-1} approximately. Actually, some authors classified these stars as a G1-G2 type (Petrov et al. [1999]) and other as a K1 type (Güdel et al. [2006]).

Chapter 4

SPIRou data

The data which we worked with derives from several nights of observation. It is relevant to note that the observations were obtained during the science verification period, before the SLS [*]. Table 4.1 shows the observation log, including the nights of observation, the respective Julian date and the indication of the band of observation, NIR and/or optical. As it is possible to see, we have three overlapped nights which allows us to perform a comparison between the NIR and optical emission lines. The optical data were obtained at the Crimean Astrophysical Observatory (CrAO) with the echelle spectrograph and spectral resolution about R∼27000, installed at the 2.6 meters Shajn reflector (Petrov et al. [2021]).

Observation night	Julian date	NIR lines	Optical lines
22/09/2018	84.0810	X	
	84.0845	X	
23/09/2018	85.0676	X	
	85.0715	X	
	85.4792		X
25/09/2018	87.0501	X	
	87.0540	X	
	87.4814		X
26/09/2018	88.0789	X	
	88.0828	X	
	88.3720		X
27/09/2018	89.3856		X

TABLE 4.1: Observation log. The Julian Date is a continuation of 24583... and it is approximated to the thousandths. The NIR observed lines are Pa 5, Pa 6, Pa 7, He I and Br 7. The optical observed lines are Hα and Na I D.

[*]This proposal was presented by R. M. Albuquerque and S. Ulmer-Moll at the final point of their PhDs.

Regarding the NIR data, we analysed the He I emission line, $\lambda = 10\,829.09$ Å, which turns out to be useful to study the structure and variability along time of the disk wind. Besides, some other emission lines such as the Paschen 5, 6 and 7 and the Brackett 7 optically thin lines are good mass accretion rate indicators, important to study the accretion variability, namely Pa 5 and Br 7 lines since they are less affected by chromospheric emission (Alcalá et al. [2014]). Paschen lines are in this way named because of the German physicist Friedrich Paschen who noticed them first in 1908 (Paschen [1908]) and Brackett lines are due to the American physicist Frederick Sumner Brackett who witnessed the spectral lines in 1922 (Brackett [1922]). With respect to the optical data, the observed spectral range include the Hα and Na I D line profiles, which are good indicators of gas flows and, thus, a useful accretion and outflow tracers. This data was obtained and kindly provided by P. Petrov, from a RY Tau monitoring between 2013 and 2019 and published in Petrov et al. [2021]. In this work we are using the optical data obtained near our NIR spectra, in time, and corresponding to four observations. Table 4.2 gathers all the analysed emission lines and their central wavelengths in the air. As mentioned before, the main reason for using this infrared band and the analysis of the Paschen, Brackett and He I lines is because those lines are usually optically thin and so the radiation is directly associated to the amount of atoms emitting in this transition. As opposed to most optical emission line, as for example Hα which is optically thick, and whose analysis is much more difficult and require the use of radiative transfer codes to get the observed profiles.

Line	Central wavelength in air (Å)
Na I D_2	5889.95
Na I D_1	5895.92
Hα	6562.80
Pa 7	10049.37
He I	10829.09
Pa 6	10938.10
Pa 5	12818.08
Br 7	21655.29

TABLE 4.2: Summary of the introduced lines with their central wavelengths.

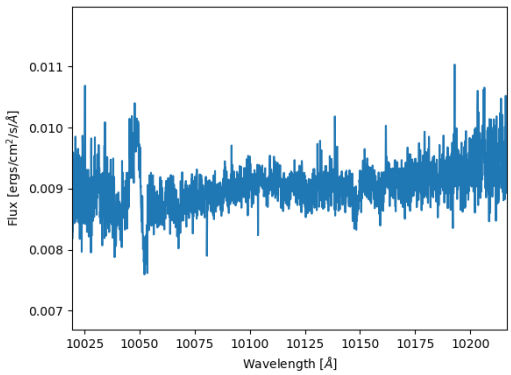

(I) 4th order, Pa 7 line.

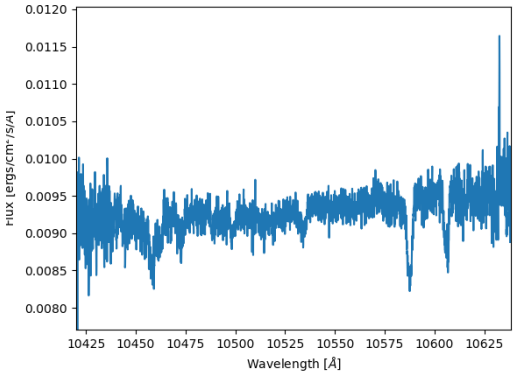

(II) 7th order.

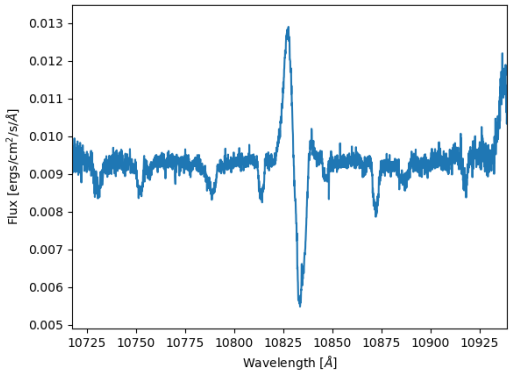

(III) 9th order, He I line.

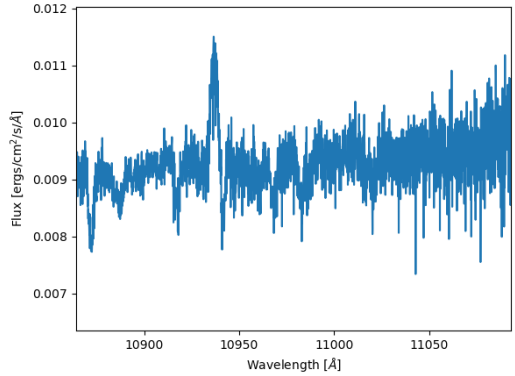

(IV) 10th order, Pa 6 line.

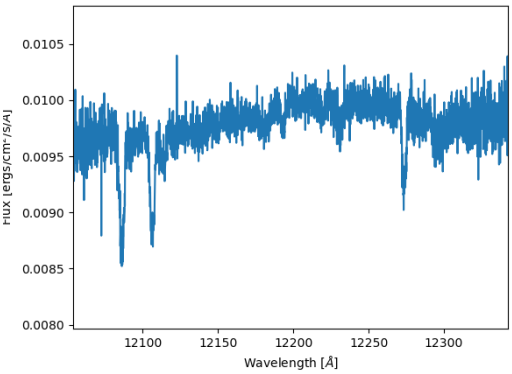

(V) 17th order.

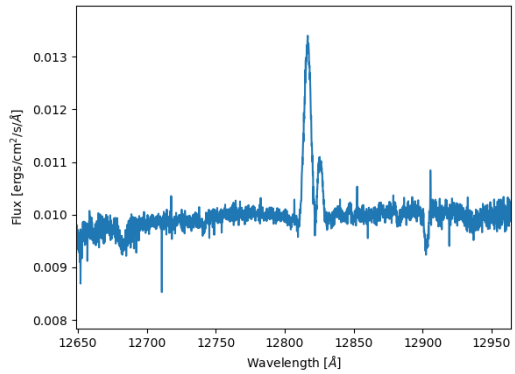

(VI) 20th order, Pa 5 line.

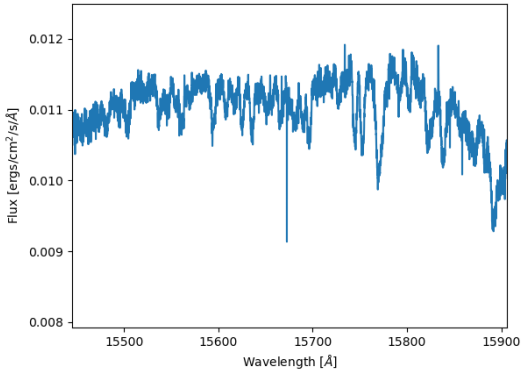

(VII) 31st order.

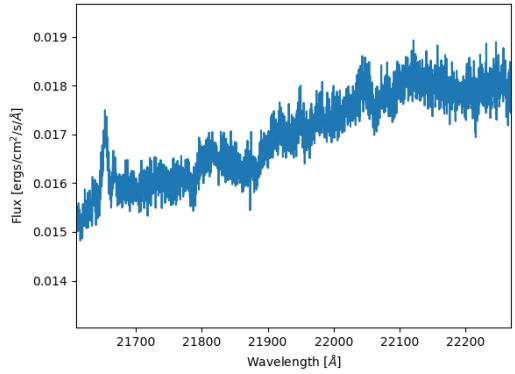

(VIII) 45th order, Br 7 line.

FIGURE 4.1: Real spectrum (without telluric lines) sampled by some of its orders. These spectra were not normalised to the continuum and are shown just as examples.

In Figure 4.1, we display a sample of several orders of the SPIRou spectrum with telluric lines removed. These spectra correspond to the first night of observation. The NIR emission lines shown in Table 4.2 are marked in the figure, as well as some intermediate orders where photospheric lines are present. Subfigures 4.1I, 4.1III, 4.1IV, 4.1VI and 4.1VIII show Pa 7, He I, Pa 6, Pa 5 and Br 7 emission lines respectively. Besides, Subfigures 4.1II, 4.1V and 4.1VII display orders with photospheric lines, useful to move the spectra to stellar rest frame and determine $v \sin i$ of the target. It is relevant to note that these spectra are not normalised to the continuum and present some noise. These issues shall be addressed in the following sections.

4.1 Data treatment

In this subsection, we introduce the treatment process performed to the data after having been reduced and the telluric lines removed, as well as, a preliminary spectral analysis.

Our goal was to obtain the residual spectra for each emission line from the original observed spectra. A residual spectrum is usually obtained by subtracting or dividing the observed spectrum by a simulated or synthetic one. In our case, the residual spectra were obtained by subtracting a synthetic spectrum of the same spectral class than the observed one. Using the residual spectra entails a vantage because we are removing the photospheric absorptions and, basically, we observe the intrinsic variations of the lines in the case the emission excess (veiling) is not very variable.

As indicated in the observation log displayed in Table 4.1, two observations were obtained per night over a few minutes. We have checked the similarities between the observations pair and determined the mean spectrum in order to increase the signal-to-noise ratio (see Figure 4.2 as an example in case of the He I emission line). Note that in the legend of this figure, we introduced the modified Julian date (MJD), given by

$$\mathrm{MJD} = \mathrm{JD} - 2400000.5, \tag{4.1}$$

where JD represents the Julian date. For the mean spectra in Figure 4.2II, we truncate the MJD value to the tenths and so we will do throughout the text for all the emission lines.

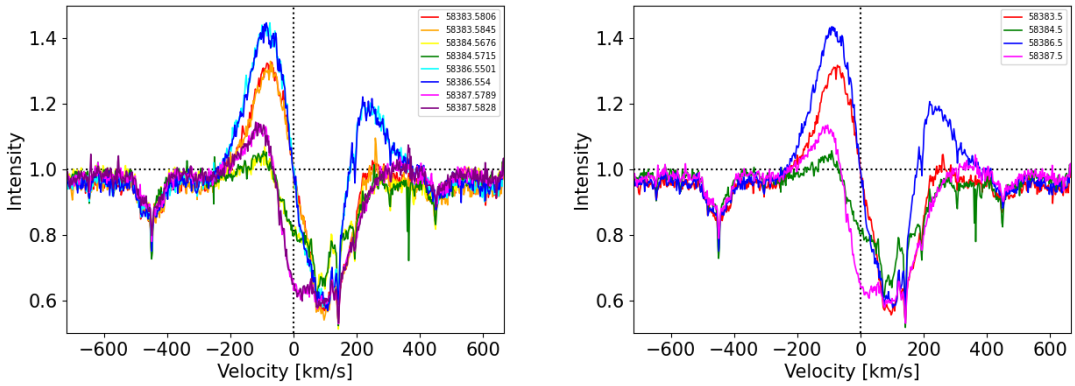

(I) Spectra considering all the observations. (II) Mean spectra.

FIGURE 4.2: He I emission line. The spectra are in the stellar rest frame with a velocity scale. The legend shows the MJD.

In order to get the residual spectra, we looked for the synthetic spectrum that best fits the observed spectra of our target. The synthetic spectrum was provided by the 'Theoretical spectra web server' * and we used the BT-Settl model grids. The free parameters of the grid are the effective temperature, the $\log(g)$ and the metallicity. The first one varies from 400 K to 70 000 K. For those values we are interested in, that is, between 4000 K and 7000 K, the step is 100 K. The $\log(g)$ varies from -0.5 to 6, with step of 0.5. The metallicity goes from -4.0 to 0.5, allowing to select the following values: -4, -3.5, -3, -2.5, -2, -1.5, -1, -0.5, 0, 0.3 and 0.5. As shown in Table 3.1 the temperature and $\log(g)$ of RY Tau, are 5945 K and 3.8, respectively. So as to download the correct synthetic spectrum, we introduced the following values for the parameters: T_{eff} between 5900 K and 6000 K, $\log(g)$ between 3.5 and 4.0 and, finally, the metallicity between -4.0 and 0.5, since we do not have much information about the metallicity of RY Tau and it is not a really relevant parameter. The BT-Settl grid displayed ten spectral files and we chose the one which fitted the best the real stellar parameters, with $T_{\text{eff}} = 5900$ K, $\log(g) = 3.5$ and metallicity equal to 0. We decided to use this synthetic template instead of a stellar spectra of similar spectral type, because the SPIRou archive is still on progress with few templates. Figure 4.3 shows a broad band of the downloaded spectrum, corresponding to the NIR band, where the emission lines which we shall address are present. The initial wavelength is $\lambda = 9557$ Å and the final wavelength is $\lambda = 25\,157$ Å, corresponding to the beginning of the first order and the ending of the forty-ninth order.

*http://svo2.cab.inta-csic.es/theory/newov2/

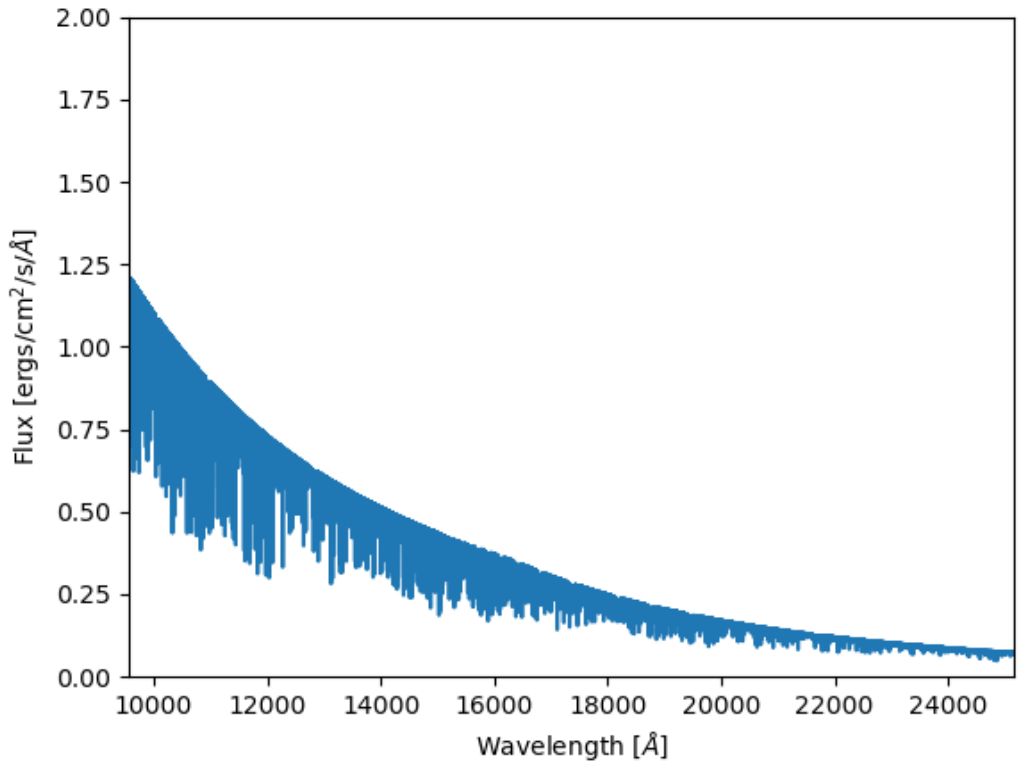

FIGURE 4.3: Synthetic spectrum from the BT-Settl in the NIR band, from $\lambda = 9557$ Å to $\lambda = 25\,157$ Å.

The selected synthetic spectrum should be processed in order to be compared with the observed one. For this purpose, we first selected just the needed wavelength intervals in our synthetic spectrum, those which we have the previous spectral lines for. Then, we obtained the broadened spectrum by performing the convolution of the rotation function with $v \sin i = 50$ km s^{-1} and the synthetic spectrum (as explained in Gray [2005]). In Figure 4.4, we show a section of the synthetic spectrum, corresponding to the 9th order of the observed spectrum, before and after applying the stellar rotation. It is patent the broadening and decrease in intensity of the photospheric lines.

In order to simulate the spectrum of our target, we convolve the broadened spectrum obtained previously with the instrumental profile, taken as a Gaussian with a Full Width at Half Maximum (FWHM) corresponding to the spectral resolution of R=60000. The spectrum obtained was finally resampled to the observed one.

Before obtaining the residual spectrum, the observed spectrum is shifted in wavelengths to get the photospheric lines in the stellar rest frame (absorption lines at the same

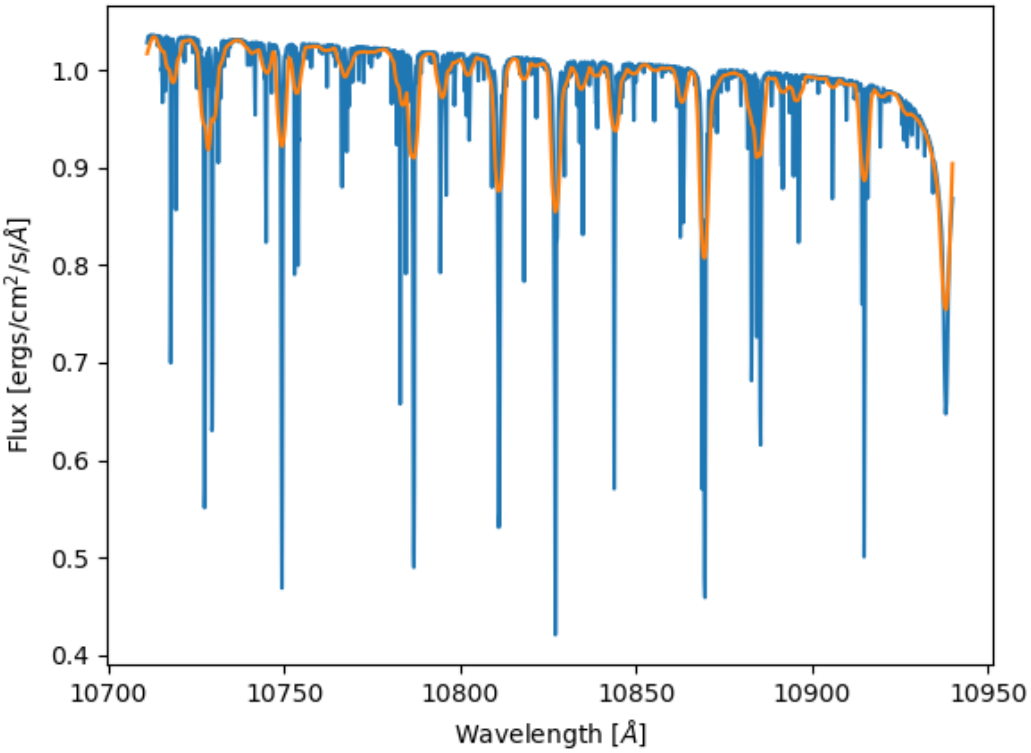

FIGURE 4.4: Synthetic flux before (blue) and after (orange) the stellar rotation simulation.

position as in the simulated spectrum). In order to do so, we created a correlation function between the observed spectra and a theoretical one obtained from the Vienna Atomic Line Database (VALD3). Then, the maximum value of the correlation function gives us the shift between the observed and simulated spectra. We did compute these values for all the orders with spectral lines except the Br 7 order, where no photospheric lines were identified. For this order, we assumed the average shift, in velocity, obtained from other orders and then we transformed it to wavelength. Table 4.3 gathers these values. The Pa 7 order shows a slightly different shift value. It was harder to compute since this line presents a lower number of photospheric lines and their quality is also worse. Figure 4.5 shows as an example the order with He I line. In panel 4.5I, we can see the simulated spectrum (orange) and the observed spectrum for the first night of observation (blue) before the shifting. In panel 4.5II, we can appreciate the shifting of the same observed spectrum according to the values shown in Table 4.3 and it is possible to see that they fit each other, displacing the observed spectrum to the stellar rest frame.

Emission line	Shift value (km s^{-1})	Shift value (Å)
He I	64.22	2.3196
Pa 5	64.06	2.7390
Pa 6	62.37	2.2755
Pa 7	82.46	2.7641
Br 7	68.28	4.9322

TABLE 4.3: Shift values between the observed and synthetic spectra.

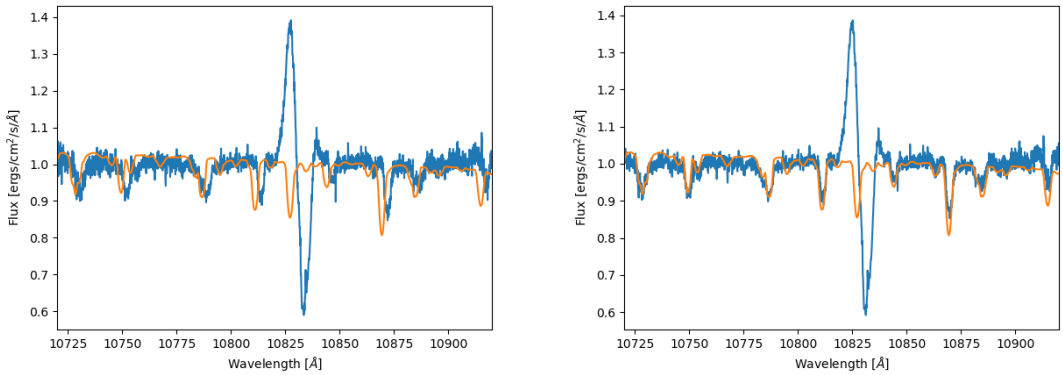

(I) Synthetic (orange) spectrum and observed (blue) spectrum before the shifting.

(II) Synthetic (orange) spectrum and observed (blue) spectrum after the shifting.

FIGURE 4.5: Comparison between the synthetic and observed spectrum for the He I line in the first night of observation (MJD: 58383.5).

After that, we performed the noise filtering and continuum normalisation for the observed spectra. The first process was carried out in order to get better spectra, that is, a cleaner flux. In order to do so, we performed a convolution of the observed spectra with a box function*, chosen to have four points, since using a small function allows us to keep the original intensity of the spectral lines. Then, the normalisation was performed using the 'specutils.fitting.fit_generic_continuum' function from 'Specutils' as well. This function works manually, in the sense that it is necessary to define several intervals as an input of the continuum and it performs a Levenberg-Marquardt algorithm and least squares statistic so as to conduct the fitting. In Figure 4.6 we can see how this normalisation process works. It is possible to see the first night of observation spectrum corresponding the 20th order (Pa 5 line) before and after the normalisation.

Then, as said before, we calculated the residual flux by subtracting the simulated spectrum to the observed one and converted the wavelength to radial velocity.

*We used the 'specutils.manipulation.box_smooth' function from 'Specutils', a package created to work with spectra.

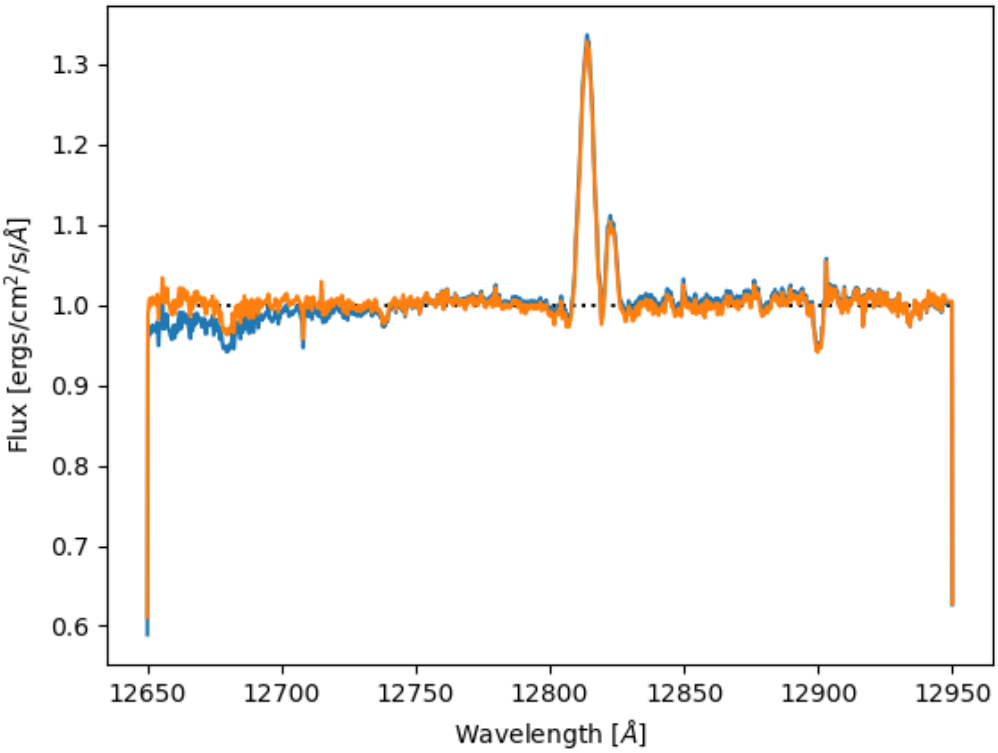

FIGURE 4.6: Observed spectrum before (blue) and after (orange) the continuum normalisation for the Pa 5 line in the first night of observation (MJD: 58383.5). The dotted line represents the continuum $y = 1$.

4.2 Spectral lines variability

First, we address Hα and Na I D line profiles, which are in the optical band and constitute a strong indicator of gas flows in the star's neighbourhood. Namely, the Hα line is usually observed for these YSOs, since it presents a strong and broad emission as a consequence of the high temperatures and velocities of the winds and matter which is in accretion (White and Basri [2003]). These temperatures have to be high enough to excite the hydrogen, producing its emission, and will depend on the density of the medium. For these CTTSs, blueshifted or redshifted absorptions overlapping broad emission lines are quite common, when the stars are undergoing some outflow and accretion processes. Usually, absorption located in the blue wing of the profile is related to stellar wind, in some cases the absorption can be seen below the continuum, obtaining a P Cygni profile, as was shown in Figure 1.5, which means that the star is experimenting a stronger outflow activity. Besides, absorption located in the red wing usually implies an accretion phenomenon, which will lead to an inverse P Cygni profile, also shown in Figure 1.5. Notice that the

terms 'blue wing' and 'red wing' refer to negative and positive values of radial velocities, respectively. Nevertheless, the system inclination could also interfere with the shape of the profiles and it is relevant to take this parameter into account.

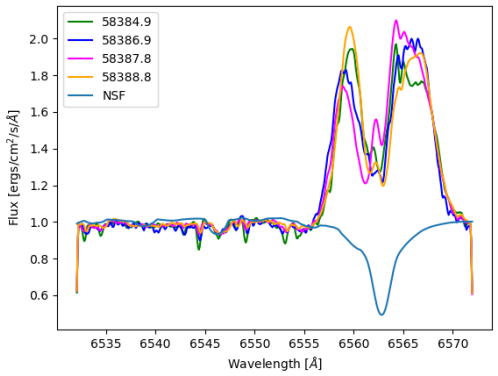

(I) Hα emission line.

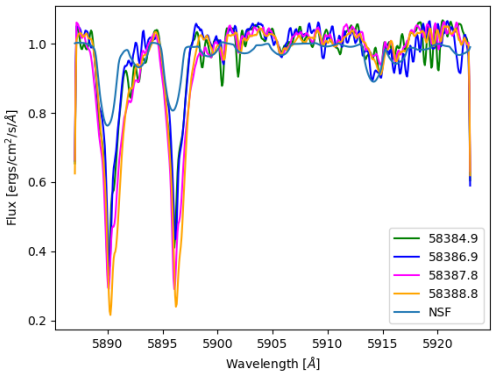

(II) Na I D line.

FIGURE 4.7: The observed optical spectra normalised to the continuum and overlapped with a simulated spectrum of the same spectral type and $v \sin i = 50$ km s^{-1} in the regions containing the Hα and Na I D lines. NSF means 'Normalised synthetic flux' and the night of observation is indicated in the legend by the MJD.

Figure 4.7 presents the Hα and Na I D lines spectra observed during four observation nights as well as the overlapped simulated spectrum rotationally broadened described in the previous section. Figure 4.8, shows the residual spectra with the continuum at 1. Notice that the photospheric lines almost disappear, the few narrow lines are telluric lines not removed in the optical. These residual spectra will be useful to us so as to perform an accretion-outflow phenomena analysis after having obtained the velocity profile, shown in Figure 4.9.

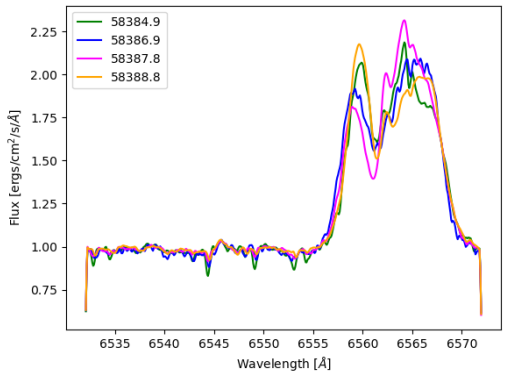

(I) Hα emission line.

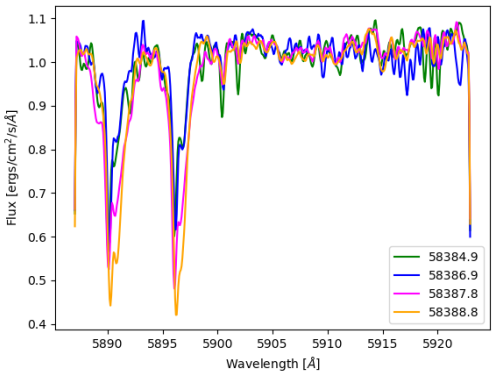

(II) Na I D line.

FIGURE 4.8: Residual spectra for the Hα and Na I D lines obtained during the four observation nights in September of 2018. The legend shows the MJD.

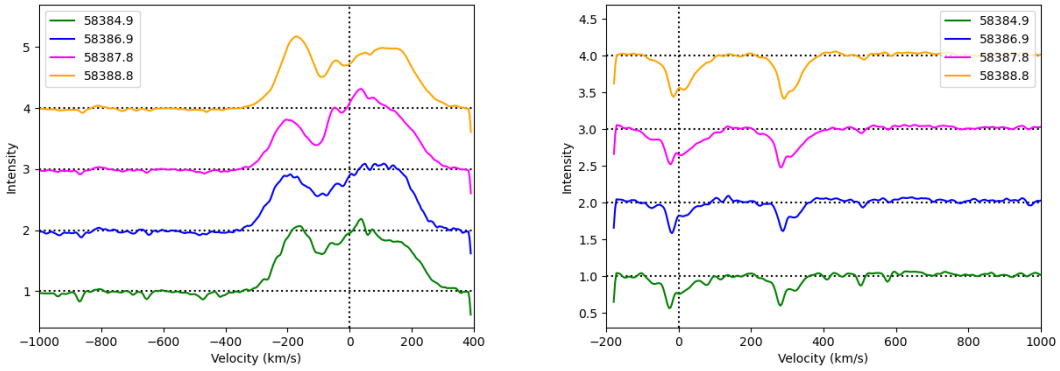

(I) Hα emission line.

(II) Na I D line.

FIGURE 4.9: Hα and Na I D lines in the stellar rest frame and velocity scale. The fluxes are normalised to the continuum and shifted vertically. The observation date is given in the legend through the MJD.

In Figure 4.9I, we present the Hα line variability in velocity scale, in order to follow the variation of the absorptions in the blue and red wings. We can observe a blueshifted absorptions superposed to the emission line near the velocity of -100 km s^{-1}. These observable absorptions are evidence of outflows, probably stellar, disk or conical winds (Petrov et al. [2019]). It is also possible to see a little occasional variation of the right wing. In Figure 4.9II, we can see the velocity profiles for the Na I D_1 and D_2 lines. Since their behaviour is practically the same, we will focus on the Na I D_2 line. Petrov et al. [2021] found that the blue and red wings of the Na I D lines change in anti-phase, that is, a rise in the blueshifted absorption is followed by a decrease of the redshifted absorption and conversely. Petrov et al. [2021] also came to the conclusion that this variation was produced each thirty days, approximately. Our observations correspond to a smaller period of time, so it is impossible to appreciate these variations. Nevertheless, we can conclude that, in our case, we are in the redshifted absorption phase, as can be seen in Figure 4.7II when comparing with the simulated spectrum in stellar standard of rest. The absorption occurs at the red part of the photospheric Na D lines, meaning that there exist infalling gas on our line of sight. Moreover, Petrov et al. [2021] also found a correlation between Hα and Na I D lines. An increase of the emission in the blue wing of Hα line is accompanied by an increase in the redshifted absorption in the Na I D lines. In our case, this fact cannot be emphatically affirmed, due to the reduced time interval of our data, as we said before.

Now, we shall address the above-mentioned NIR band line profiles, that is, He I, Pa 5, Pa 6, Pa 7 and Br 7. As said before, these are good accretion tracers (Edwards et al. [2006]) and can also be used to monitor outflows (Kwan et al. [2007]).

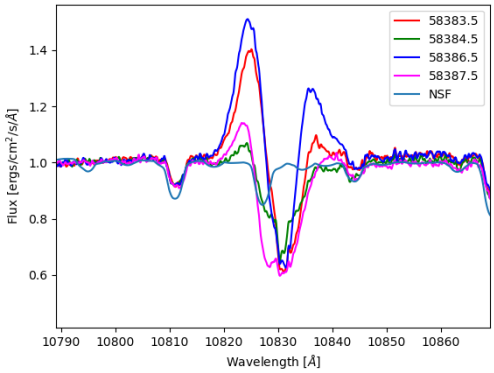

(I) He I emission line.

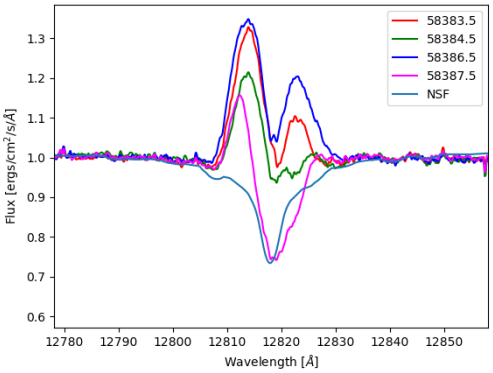

(II) Pa 5 emission line.

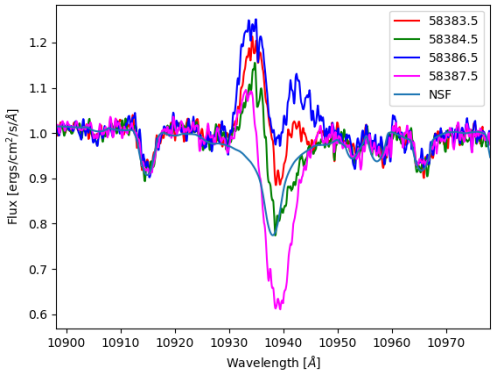

(III) Pa 6 emission line.

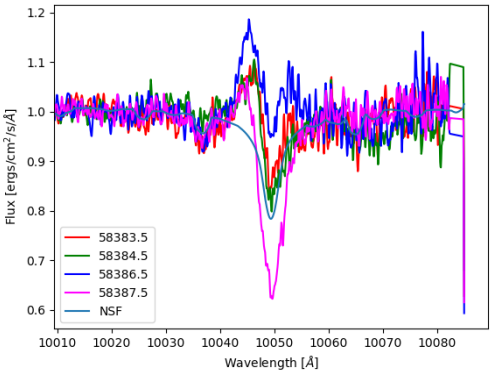

(IV) Pa 7 emission line.

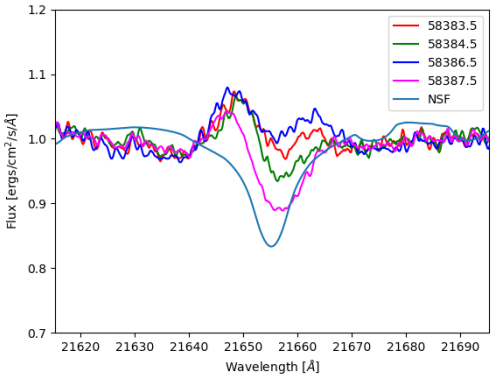

(V) Br 7 emission line.

FIGURE 4.10: The observed NIR spectra normalised to the continuum and overlapped with a simulated spectrum of the same spectral type and $v \sin i = 50$ km s^{-1} in the regions containing the main emission lines. NSF means 'Normalised synthetic flux' and the night of observation is indicated in the legend by the MJD.

In Figure 4.10, we display the average spectrum obtained per night overlapped with the corresponding synthetic spectrum with adequate resolution and rotationally broadened. In Figure 4.11 we show the residual spectra obtained as the subtraction of synthetic spectrum after the match of the position of the photospheric lines.

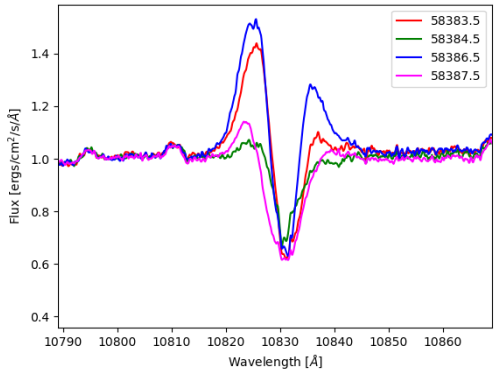

(I) He I emission line.

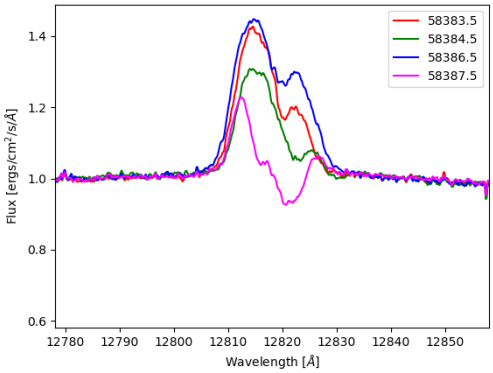

(II) Pa 5 emission line.

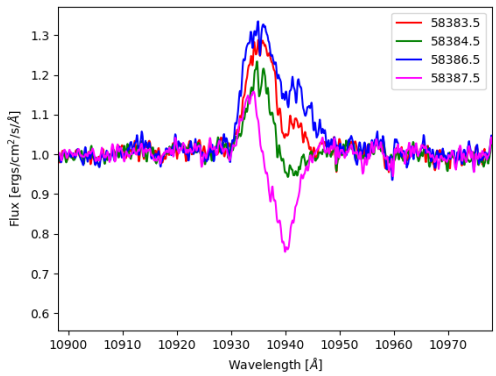

(III) Pa 6 emission line.

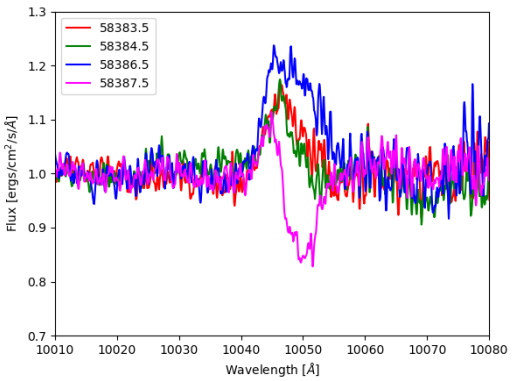

(IV) Pa 7 emission line.

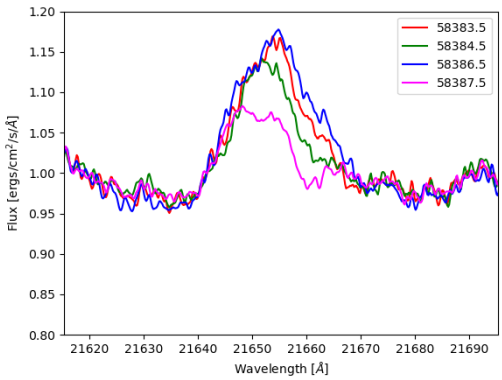

(V) Br 7 emission line.

FIGURE 4.11: Residual spectra for the NIR emission in RY Tau during the four observation nights in September of 2018. The legend shows the MJD.

The emission lines variations are also displayed in Figure 4.12 with xx axis in velocity scale, allowing the dynamics study of the matter that are emitting. In the following lines, we shall address an analysis so as to draw conclusions about accretion an outflow activity in this RY Tau star.

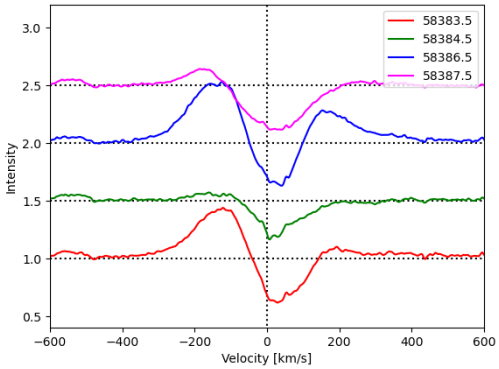

(I) He I emission line.

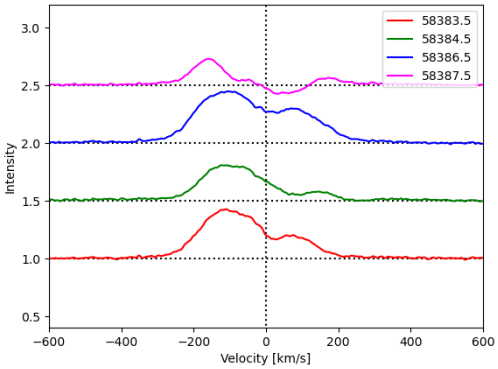

(II) Pa 5 emission line.

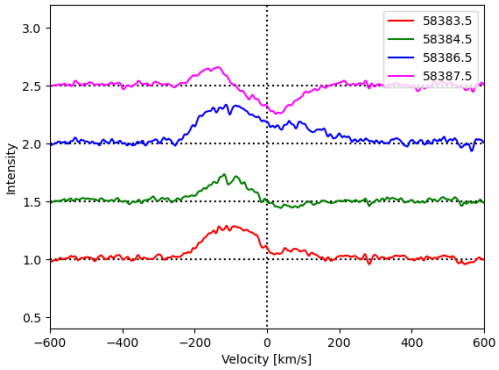

(III) Pa 6 emission line.

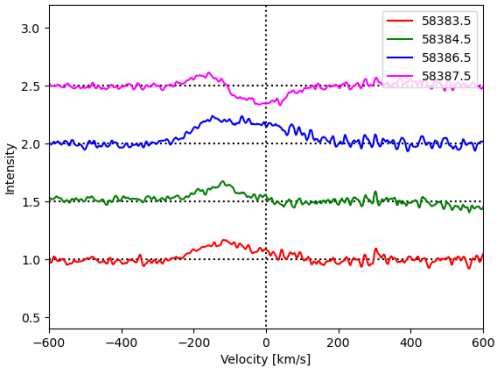

(IV) Pa 7 emission line.

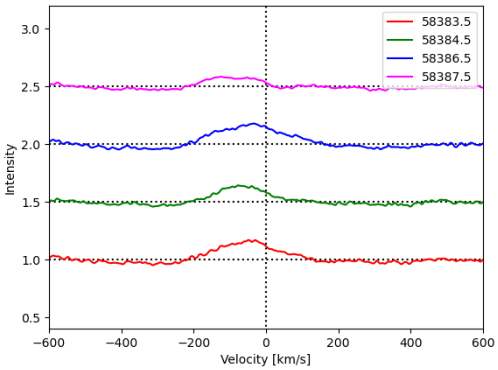

(V) Br 7 emission line.

FIGURE 4.12: Velocity profiles for the NIR emission in RY Tau during four nights in September of 2018. The fluxes are normalised to the continuum and shifted vertically. The spectra are in the stellar rest frame with a velocity scale. The legend shows the MJD.

In Figure 4.12I, it is completely clear the daily variability of the flux as well as the intensity and shift of the absorption in the red wing of the He I line. In that case, such absorption goes under the continuum line, leading to an inverse P Cygni profile, indicating a substantial accretion activity, in other words, it is indicative of high amount of mass

infall. This line profile is thought to be originated in magnetic loop of the magnetosphere near the stellar surface, confirmed by the redshifted absorption (Hartmann et al. [1994]). The average velocity of the redshifted absorption is relatively stable, suggesting no strong variation of the magnetic topology during these four nights. This He I line also presents a high potential to diagnose outflows, since about 70 % of the studied CTTSs profiles, show blueshifted absorption (Edwards et al. [2006], Kwan et al. [2007]). Nevertheless, it does not occur in our case, possibly as a consequence of the quasi edge-on observation of RY Tau.

The variability of the three observed Paschen lines is quite similar as shown in Figure 4.12II, 4.12III and 4.12IV. The overlapped redshifted absorption is not as intense as in the Helium line but we see a clear daily variation of the profiles shape. The last night of observation, the 26th of September (MJD: 58387.5), the inverse P Cygni profile is more pronounced, suggesting an increase of the mass accretion rate during this night.

The Brackett line has a similar behaviour to the ones of Paschen lines as seen in Figure 4.12V. We notice a daily variability and a weak redshifted absorption that change the line profile. Again in the last night of observation, the redshifted absorption is clearly more intense.

In summary, we can say that the daily variability is fully clear for all the studied emission lines in both optical and NIR bands. The profiles changes in the NIR lines take place essentially in the red wing of the profiles indicating an intense and variable accretion activity. The intensity variation of the redshifted absorption can be related to the mass accretion rate change. The main variations in the Na D lines are also in the red wing but in the case of the Hα line, despite there is some variation also in the red wing, the biggest variability is present in the blue wing. This suggest that most of the absorption observed in the Na D lines are due to the matter in the magnetic loop that connect the inner part of the disk and the star. In the case of the Hα line, the absorptions trace the stellar or disk outflows.

4.3 Equivalent width analysis

In this subsection, we shall address an analysis of the lines equivalent widths and possible correlations between different lines. This shall allow us to quantify the lines variability and check for any relation between accretion and outflow. The possible knowledge of

the star magnitudes in the optical and NIR bands will also provide us the lines flux determination. This will be important to quantify the variability of the mass accretion rate (de Albuquerque et al. [2020]). However over our time range of observation no photometry was obtained in the NIR. In the optical range, P. Petrov kindly provided us some magnitudes measurements of RY Tau during September 2018 as shown in Table 4.4. Between nights 23th and 26th the average variation is about or less than 0.1 mag. The total flux radiated in the line is obtained as $F = EW \times 10^{-0.4(m_V - 10)}$, where the flux is expressed in units of the continuum flux of a star with $m_V = 10$ mag (which corresponds to a flux of 3.67×10^{-13} erg cm^{-2} s^{-1} Å^{-1}) (e.g. Petrov et al. [2021]). A precision in magnitude of 0.1 corresponds to an error in flux less than 5%. We assume that this variation is small and equivalent widths variations are essentially due to intrinsic changes in the profiles. A much higher variation occur in night 27th with an increase of the stellar brightness in the three bands.

Observation night	MJD	V mag	R mag	I mag
23/09/2018	58385.08	9.946	8.860	7.007
26/09/2018	58388.07	9.922	8.805	6.89
27/09/2018	58389.07	9.799	8.684	6.791

TABLE 4.4: V, R and I magnitude values for RY Tau during the nights of observation from which we have available data.

First, we will introduce the concept of equivalent width of a spectral line, which is used to measure the area of such line by creating a rectangle whose height equals the continuum's and whose width is such that the rectangle area is equal to the area of the spectral line (Carroll and Ostlie [2017]). Formally, the equivalent width is given by

$$W_\lambda = \int \left(1 - \frac{F_\lambda}{F_0}\right) \mathrm{d}\lambda, \tag{4.2}$$

where F_λ represents the flux at a given wavelength and F_0 the continuum flux, taken as constant over the line (Stahler and Palla [2004]). Figure 4.13 illustrates the notion of equivalent width. Let's note that, when we analyse the values of the equivalent width afterwards, there will be positive and negative values. By definition, the equivalent width of an emission line is negative and positive in the case of an absorption line.

Our main purpose here is not only the equivalent width itself, but to quantify the normalised emission of a line in a given range band of velocities. In this way, we can quantify and compare the variability of the red and blue wings of each line (Petrov et al. [2019]).

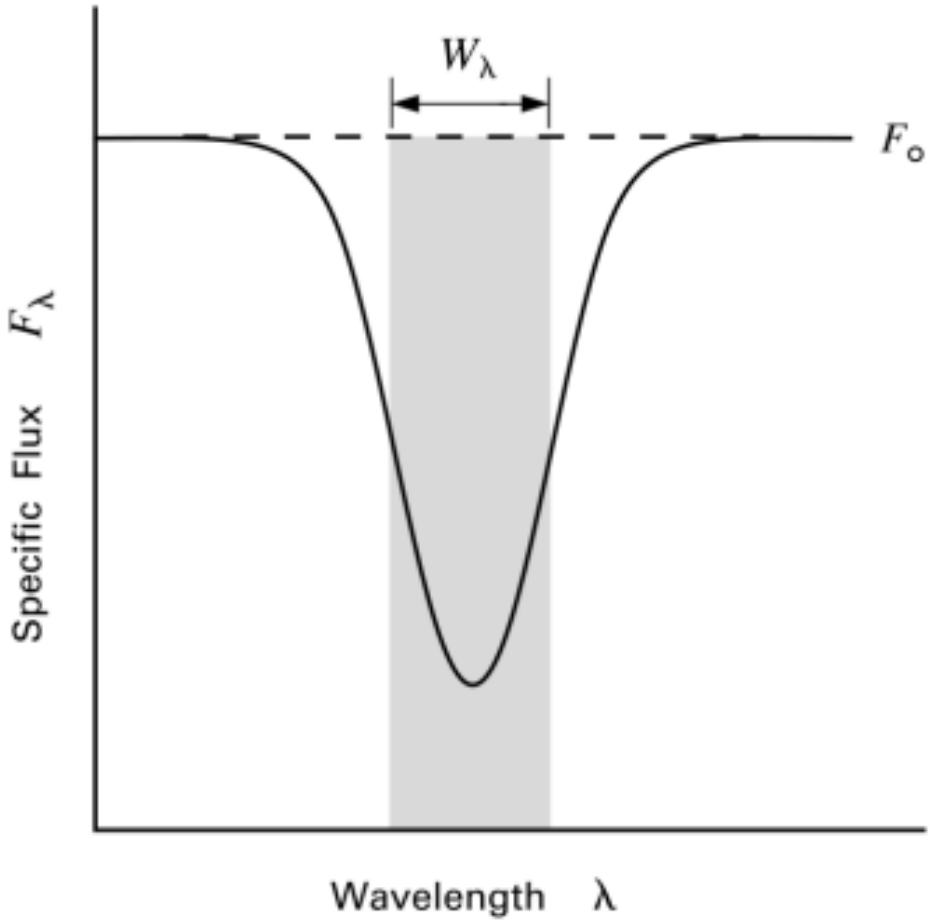

FIGURE 4.13: Illustration of the equivalent width definition considering an absorption line. F_0 represents the continuum flux. From Stahler and Palla [2004].

From the obtained residual spectra, we calculated the band equivalent widths for each emission line, over the four nights. We considered three bands according to radial velocity limits: blue, red and full. The choice of the limits which delimit those bands are line dependent. The bands limits reflect the main variations in the red and blue profiles shape.

First, we shall address the optical lines and then the lines from the NIR. However, we shall introduce now the procedure of calculating the equivalent width, since it is the same for all the emission lines. The first step was to define the three bands limits and, henceforth, using the 'Specutils' package as before, to calculate the equivalent width with the 'equivalent_width' function. Note that we are most of all interested in blue and red bands since those are the ones related to outflow and accretion activity.

4.3.1 Hα and Na I D lines

For the Hα emission line, we used the following limits for each band: the blue band goes from -200 km s^{-1} to -25 km s^{-1} and the red one goes from 25 km s^{-1} to 200 km s^{-1}. We considered the full line from -350 km s^{-1} to 350 km s^{-1}. Figure 4.14 shows the two considered blue and red bands superposed to the residual spectra for the Hα emission line.

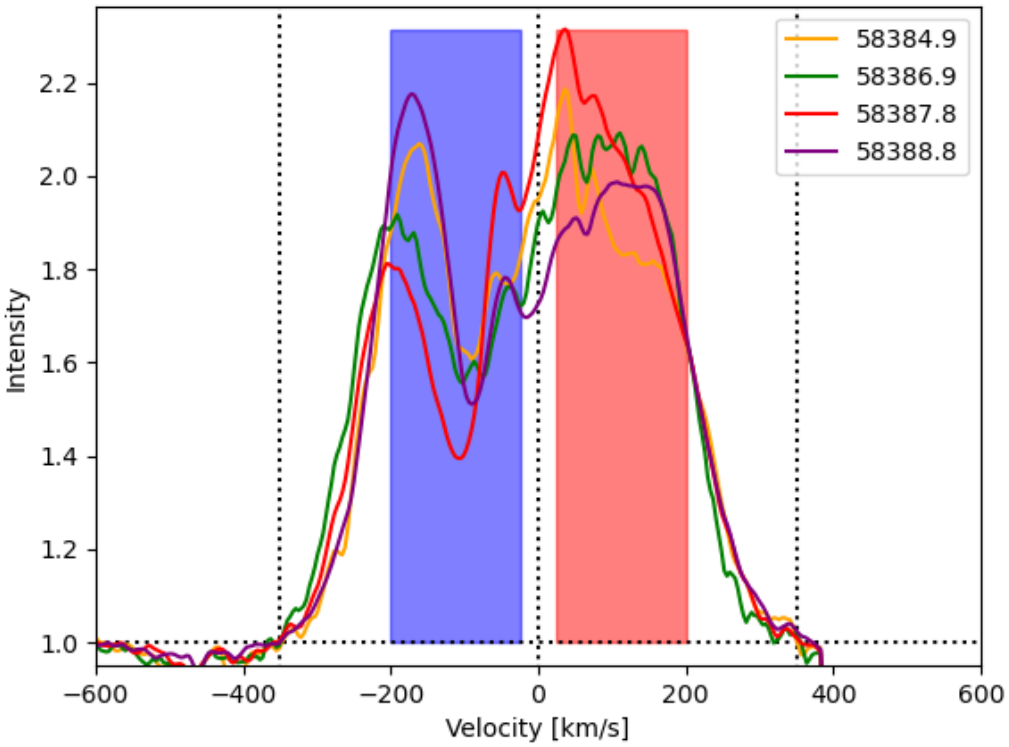

FIGURE 4.14: Hα emission lines obtained during the four nights with the blue and red bands superposed. The dotted lines indicate the profile limit in the stellar rest frame coordinates and in the legend we indicate the MJD.

Furthermore, Table 4.5 shows the bands equivalent width values for this emission line, set out by night and band. It also displays the estimated error. This error was calculated by assuming a continuum relative precision of 1%. As a consequence, we obtained two new spectra, one by underestimating the continuum by 1% and the other for overestimating it by 1%. By calculating the equivalent width of these two new lines from the new spectra, we obtained two new values which allowed us to estimate the absolute error in

the equivalent width determination as follows

$$\Delta W_\lambda = \left| W_{\lambda,-1\%} - W_{\lambda,+1\%} \right| . \tag{4.3}$$

MJD	Blue	Red	Full
58384.9	-3.26 ± 0.14	-3.47 ± 0.14	-9.38 ± 0.49
58386.9	-2.82 ± 0.13	-3.90 ± 0.15	-9.53 ± 0.50
58387.8	-2.68 ± 0.13	-4.03 ± 0.16	-9.63 ± 0.50
58388.8	-3.31 ± 0.14	-3.61 ± 0.15	-9.38 ± 0.49

TABLE 4.5: Blue and red equivalent widths values for the Hα line, expressed in Å. The last column gives the total equivalent width. Errors are also included.

Regarding Na I D, we will focus only in the Na I D_2 line as well, because of the same reason as before. The limits used for Na I D_2 line are the following: the blue band goes from -160 km s^{-1} to -40 km s^{-1} and the red one goes from 10 km s^{-1} to 160 km s^{-1}. We chose the full line limits to be -160 km s^{-1} and 160 km s^{-1}. In this case, the choice of the limits was conditioned by the telluric line around 20 km s^{-1} during the four nights, as can be seen in Figure 4.15. We selected the higher limit of the blue band so that this band does not include such atmospheric line. Figure 4.15 illustrates these bands superposed to the four residual spectra for the Na I D_2 line.

Tables 4.6 and 4.7 gather the equivalent width of Na I D lines. For Na I D_2 line and in the red band, negative and positive values are available, depending whether the weight of intensities in absorption or emission.

MJD	Blue	Red	Full
58384.9	0.02 ± 0.05	0.12 ± 0.05	0.50 ± 0.11
58386.9	-0.05 ± 0.05	-0.01 ± 0.06	0.26 ± 0.12
58387.8	0.09 ± 0.05	0.27 ± 0.05	0.79 ± 0.11
58388.8	-0.03 ± 0.05	0.31 ± 0.05	0.78 ± 0.11

TABLE 4.6: Equivalent width values [Å] by night and band for the Na I D_2 line. Errors are also included.

MJD	Blue	Red	Full
58384.9	-0.05 ± 0.04	0.04 ± 0.06	0.29 ± 0.11
58386.9	-0.07 ± 0.04	0.01 ± 0.06	0.18 ± 0.11
58387.8	-0.01 ± 0.04	0.29 ± 0.05	0.65 ± 0.10
58388.8	-0.04 ± 0.04	0.31 ± 0.05	0.63 ± 0.10

TABLE 4.7: Equivalent width values [Å] by night and band for the Na I D_1 line. Errors are also included.

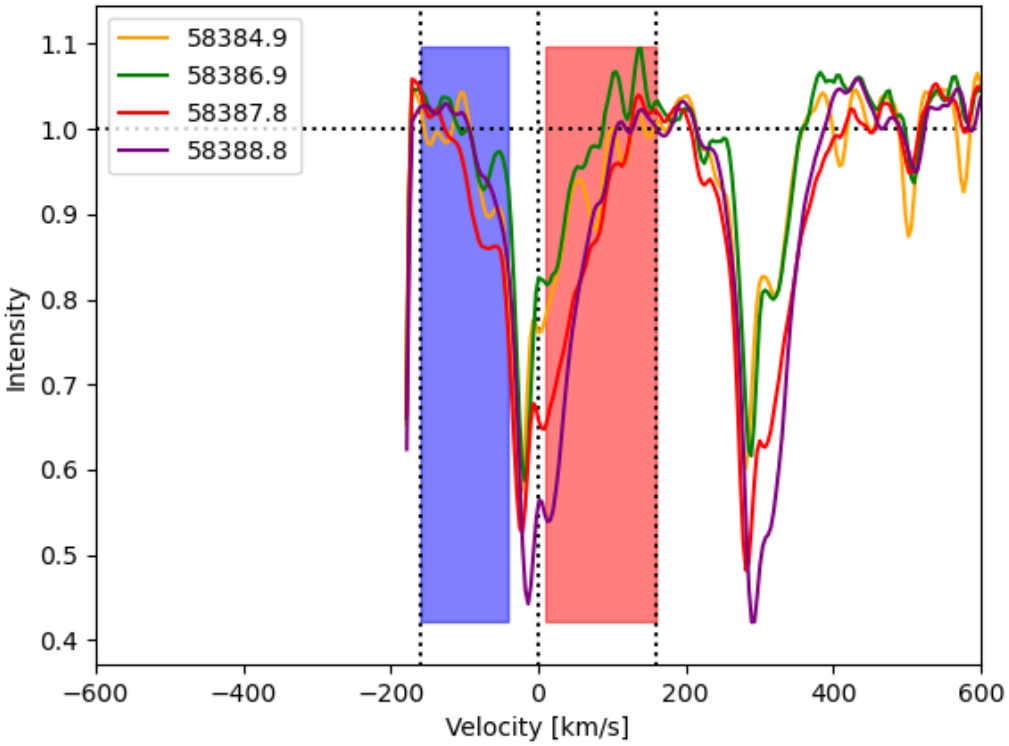

FIGURE 4.15: Velocity profile for the Na I D_2 line with the blue and red bands superposed. The dotted lines indicate the limits of the profile and the zero velocity corresponds to the stellar rest frame. The legend shows the MJD. A similar procedure has been taken for the Na I D_1 line.

4.3.2 He I line

For the He I emission line, we used the following limits for the bands: the blue band goes from -300 km s^{-1} to -10 km s^{-1}, the red band goes from 10 km s^{-1} to 200 km s^{-1} and the full line was considered from -380 km s^{-1} to 380 km s^{-1}. Figure 4.16 shows the two bands superposed to the residual spectra for the He I emission line.

Table 4.8 gathers the equivalent width values for the He I emission line organised by night and band.

Night \Band	Blue	Red	Full
MJD: 58383.5	-2.32 ± 0.25	1.00 ± 0.12	-1.43 ± 0.58
MJD: 58384.5	-0.14 ± 0.21	0.96 ± 0.12	1.10 ± 0.53
MJD: 58386.5	-2.88 ± 0.26	0.04 ± 0.13	-3.42 ± 0.62
MJD: 58387.5	0.10 ± 0.20	1.49 ± 0.11	1.78 ± 0.51

TABLE 4.8: Equivalent width values [Å] by night and band for the He I emission line. Errors are also included.

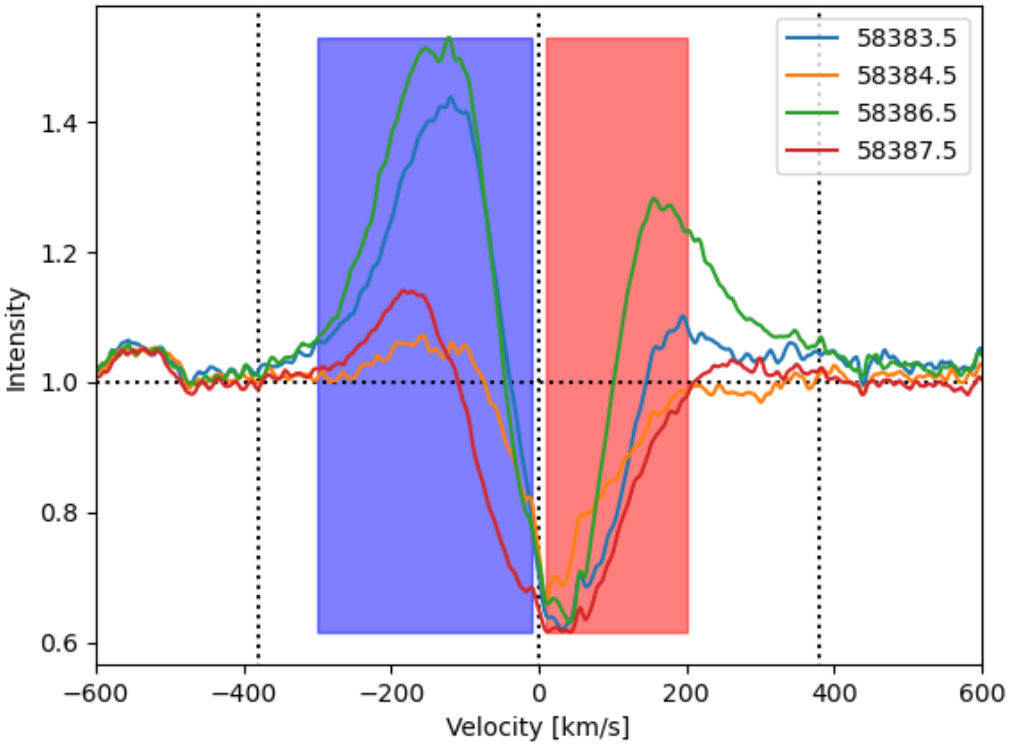

FIGURE 4.16: Velocity profile for the He I emission line with the blue and red bands superposed. The dotted lines indicate the limits of the profile and the zero velocity corresponds to the stellar rest frame. The legend shows the MJD of each observation.

Figure 4.17 shows the evolution of the equivalent width values during the four observation nights. We notice that the variability of the line correlates with the variability in the blue band. When the equivalent width in the blue band increases, the same occurs for the full band. This correlation is not seen in the red band because we trace only the superposed strong redshifted absorption. Notice that the emission at the far red wing is well related with the variability in the blue band. When the equivalent width in the blue band increases, it is caused by a higher amount of matter falling into the star and, as a consequence, this infall prevents from observing the outflowing matter, originating an increase of the equivalent width in the red wing.

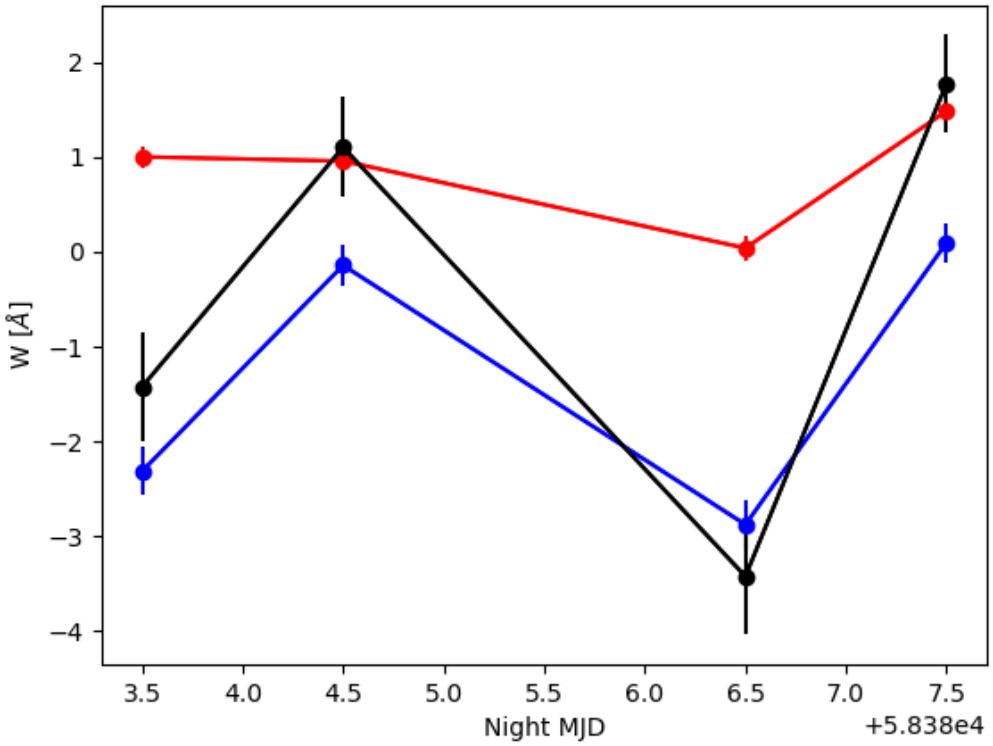

FIGURE 4.17: Equivalent widths evolution during the four nights of observation for the He I emission line. The colours indicate the blue, red and full (black) bands. The error bars are included.

4.3.3 The Paschen and Brackett lines

For the three Paschen emission lines, the bands limits are similar but we considered different values for them, according to the shape of the profile. The blue band goes from -200 km s^{-1} to -25 km s^{-1} for the Pa 5 and Pa 6 lines and from -170 km s^{-1} to -25 km s^{-1} for the Pa 7 line. Regarding the red band, it goes from 25 km s^{-1} to 230 km s^{-1} for the Pa 5 line, from 25 km s^{-1} to 220 km s^{-1} for the Pa 6 line and from 25 km s^{-1} to 170 km s^{-1} for the Pa 7 line. The full line limits were also defined for each case, from -400 km s^{-1} to 300 km s^{-1} for the Pa 5 line, from -260 km s^{-1} to 260 km s^{-1} for the Pa 6 line and from -230 km s^{-1} to 230 km s^{-1} for the Pa 7 line. Figures 4.18I, 4.18II and 4.18III show the above-mentioned limits superposed to the residual profile of the three emission lines. Tables 4.9, 4.10 and 4.11 contain the equivalent width values for these three emission lines.

Finally, we shall address the equivalent width analysis for the Brackett 7 line. Here, we chose the following bands limits: from -150 km s^{-1} to -20 km s^{-1} for the blue band, from 30 km s^{-1} to 170 km s^{-1} for the red band and from -200 km s^{-1} to 200 km s^{-1} for

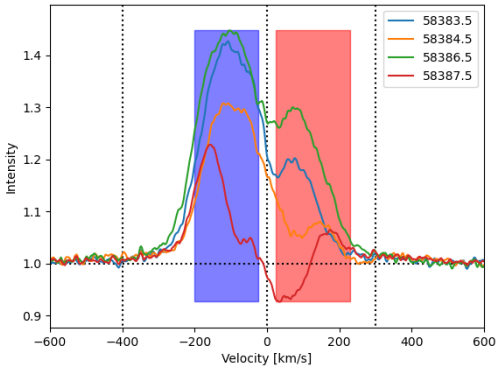

(I) Paschen 5

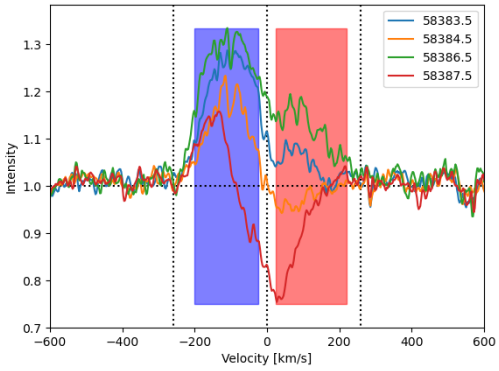

(II) Paschen 6

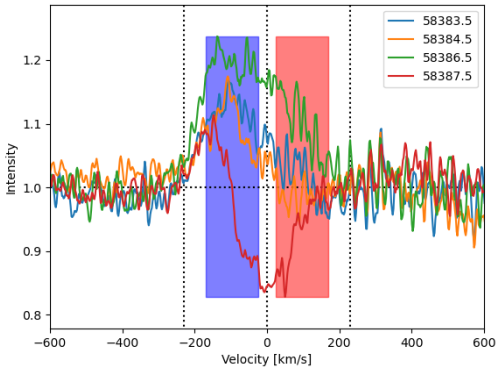

(III) Paschen 7

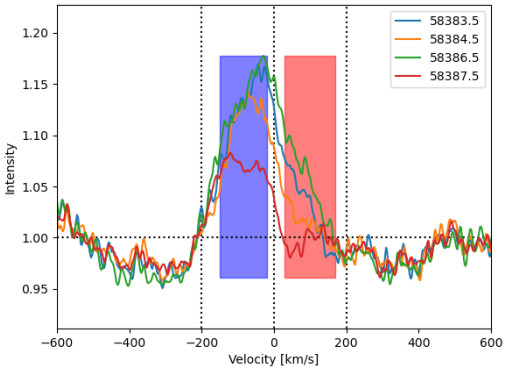

(IV) Brackett 7

FIGURE 4.18: Velocity profiles for the Pa 5, Pa 6, Pa 7 and Br 7 lines with the blue and red bands superposed. The dotted lines indicate the limits of the profile and zero velocity corresponds to the rest stellar frame. The legend shows the MJD of each observation.

Night \Band	Blue	Red	Full
MJD: 58383.5	-2.76 ± 0.20	-1.14 ± 0.20	-4.70 ± 0.69
MJD: 58384.5	-2.04 ± 0.19	-0.64 ± 0.19	-3.23 ± 0.66
MJD: 58386.5	-3.02 ± 0.21	-1.90 ± 0.21	-6.03 ± 0.71
MJD: 58387.5	-1.01 ± 0.17	-0.09 ± 0.18	-1.27 ± 0.62

TABLE 4.9: Equivalent width values [Å] by night and band for the Pa 5 emission line. Errors are also included.

the full one. In Figure 4.18IV, we can see these bands superposed to the residual spectra corresponding to the Br 7 emission line and Table 4.12 shows the values of the equivalent width by night and band for this emission line.

Night \Band	Blue	Red	Full
MJD: 58383.5	-1.56 ± 0.16	-0.39 ± 0.15	-2.17 ± 0.42
MJD: 58384.5	-1.01 ± 0.15	0.07 ± 0.14	-0.93 ± 0.40
MJD: 58386.5	-1.83 ± 0.16	-0.94 ± 0.16	-3.21 ± 0.44
MJD: 58387.5	-0.37 ± 0.13	0.45 ± 0.03	0.43 ± 0.37

TABLE 4.10: Equivalent width values [Å] by night and band for the Pa 6 emission line. Errors are also included.

Night \Band	Blue	Red	Full
MJD: 58383.5	-0.66 ± 0.11	-0.14 ± 0.10	-0.91 ± 0.33
MJD: 58384.5	-0.55 ± 0.11	-0.01 ± 0.10	-0.67 ± 0.32
MJD: 58386.5	-1.02 ± 0.12	-0.54 ± 0.11	-2.02 ± 0.35
MJD: 58387.5	-0.01 ± 0.10	0.23 ± 0.09	0.47 ± 0.30

TABLE 4.11: Equivalent width values [Å] by night and band for the Pa 7 emission line. Errors are also included.

Night \Band	Blue	Red	Full
MJD: 58383.5	-1.39 ± 0.21	-0.47 ± 0.21	-2.18 ± 0.62
MJD: 58384.5	-1.25 ± 0.21	-0.31 ± 0.20	-1.71 ± 0.61
MJD: 58386.5	-1.47 ± 0.21	-0.71 ± 0.21	-2.66 ± 0.63
MJD: 58387.5	-0.85 ± 0.20	-0.15 ± 0.20	-1.03 ± 0.59

TABLE 4.12: Equivalent width values [Å] by night and band for the Br 7 emission line. Errors are also included.

Figure 4.19 shows the evolution of the equivalent width values by night and band for Paschen and Brackett emission lines. It is easy to see that all of them behave in the same way for both bands, there exist an increase of the equivalent width from the first to the second night, then a decrease is produced and, finally, the equivalent width grows again from the third to the fourth night. Despite Br 7 line presents a softer variation, the general behaviour is the same that for the Paschen lines. This similar behaviour is expected, since we are dealing with the element hydrogen and the lines should be produced in neighbouring regions.

Now, let's also consider the He I and optical lines. Figure 4.20 shows all the lines. The equivalent width values of the He I present a similar general behaviour compared to the Paschen and Brackett ones. In the blue band, He I equivalent width also increases from the first to the second night, then falls in the third night and, finally, grows again. Regarding the red band, the behaviour remains the same, except from the transition from the first to the second night, which does not show a clear increase. As it is possible to see, the equivalent width of the Na I D_2 line behaves similarly to the NIR lines, despite the

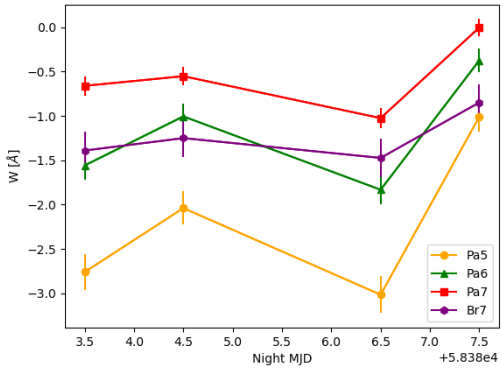

(I) Blue band.

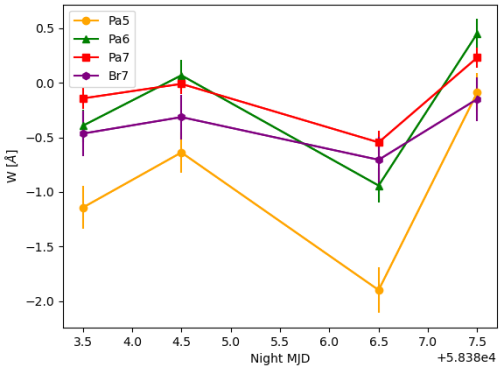

(II) Red band.

FIGURE 4.19: Equivalent width value evolution during the four nights of observation for the Paschen and Brackett emission lines.

variation of the equivalent width is much more softer because of its small values. Regarding Hα line, the behaviour is different from the other lines. In the red band, when all lines present the maximum value of their equivalent width, Hα shows its minimum value, on MJD: 58387.8. As we have previously seen in this chapter, the NIR lines show their maximum of absorption in their red wing on this night, while Hα presents its maximum of absorption on the blue wing. This inverse correlation means that the accretion indicated by the redshifted absorption (shown in the NIR lines) is followed by some intense outflow phenomena, indicated by the blueshifted absorption in Hα line. It makes sense in terms of timing, since, as it was said before, the observation in the optical band were performed about ten hours later than the NIR observations.

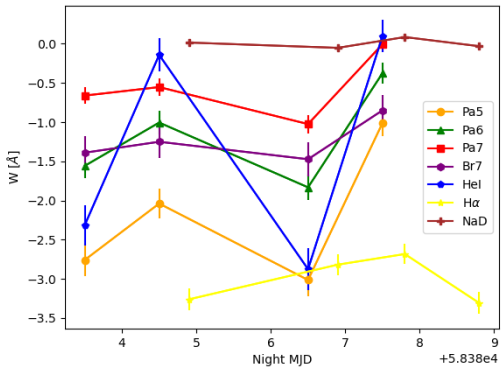

(I) Blue band.

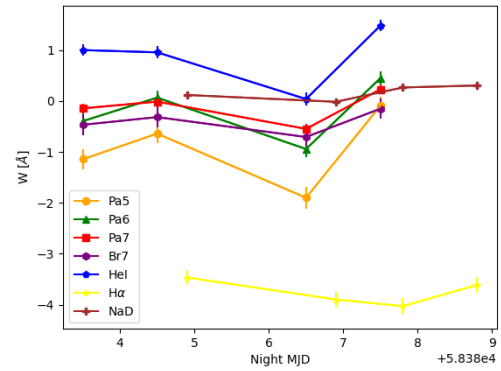

(II) Red band.

FIGURE 4.20: Equivalent width value evolution during the four nights of observation for the Paschen, Brackett, He I, Hα and Na I D_2 lines.

4.3.4 Comparison among lines

A possible way to study the variability between different lines and bands could be the analysis of relative variations. The band equivalent widths values shown in Tables 4.5, 4.6, 4.8, 4.9, 4.10, 4.11 and 4.12 allowed us to calculate the equivalent width relative variation to one of the nights of observation. The elected night was the corresponding to MJD: 58384, since it is the first common night between optical and NIR observations. Let's note that both observations are not simultaneous, the NIR lines are observed first and the optical lines about seven to ten hours later, but this fact will not considerably affect our analysis. So, the equivalent width relative variation was computed as follows

$$W'_i = \frac{W_i - W_0}{W_0}, \tag{4.4}$$

where W'_i represents the relative equivalent width variation of the ith night to MJD: 58384.5 (NIR) or MJD: 58384.9 (optical) night. W_i is the line equivalent width of the ith night and W_0 represents the equivalent width value of the reference night. This was performed by band and the results are gathered in the following tables.

Table 4.13 shows the relative variation of the Hα equivalent width values with respect to the first night of observation in the optical band. The errors made in their calculation are also shown. These errors were computed as follows

$$\Delta\left[\frac{W_i - W_0}{W_0}\right] = \Delta\left[\frac{W_i}{W_0} - 1\right] = \Delta\left(\frac{W_i}{W_0}\right) = \frac{\Delta W_i}{W_0} + \frac{W_i}{W_0^2}\Delta W_0. \tag{4.5}$$

Night variation	Blue band	Red band
58386.9 / 58384.9	0.1358 ± 0.0774	0.1244 ± 0.0910
58387.8 / 58384.9	0.1773 ± 0.0748	0.1626 ± 0.0933
58388.8 / 58384.9	0.0145 ± 0.0869	0.0417 ± 0.0859

TABLE 4.13: Equivalent width variations relative to the first night for the Hα emission line. Errors are also included.

The data gathered in Table 4.13, as well as Figure 4.14, indicate that the third night (MJD: 58387.8) flux is the one which varies the most in relation to the reference night, independently of the considered band. Moreover, the flux corresponding to the last night (MJD: 58388.8) presents a very slight variation, which is relevant since it means that the line went back to a previous state. Finally, it is important to note that the variation in the blue and red wings is bigger in the same day, corresponding to the third night, although the red wing flux does not get back to the previous state as the blue wing does. We can

conclude that there exists a notable variability in both wings even though it is hard to know if they are related.

Now, Table 4.14 shows the calculated values of the equivalent width variation for the Na I D_2 line.

Night variation	Blue band	Red band
58386.9 / 58384.9	4.2248 ± 6.2087	1.1135 ± 0.4267
58387.8 / 58384.9	4.3894 ± 18.0773	1.2220 ± 1.4456
58388.8 / 58384.9	2.9210 ± 2.5467	1.5488 ± 1.5881

TABLE 4.14: Equivalent width relative variation in relation to the first night value by band for the Na I D_2 line. Errors are also included.

As before, we can draw some results from the data in Table 4.14 and Figure 4.15. In relation to the blue band, there are some variations, being the third night flux the one which diverges the most. Regarding the red band, the last night is the one which presents a higher variability, as can be seen in Figure 4.15 and in Table 4.14. Let's note that some values of the equivalent width variation, as well as the associated errors, are extremely big. This is caused because of very small equivalent width value of the reference night and it is senseless trying to interpret them.

From the data in Table 4.8, we also computed the values of the relative variation for He I line. Table 4.15 shows these values. Let's remember that for the NIR emission lines, we compute the variation regarding the second night value because that night is the first for the optical data and, thus, we can compare them.

Night variation	Blue band	Red band
58383.5 / 58384.5	15.3858 ± 26.3068	0.0465 ± 0.2490
58386.5 / 58384.5	19.3613 ± 32.3199	0.9575 ± 0.1456
58387.5 / 58384.5	1.6923 ± 0.4148	0.5511 ± 0.3010

TABLE 4.15: Equivalent width relative variation in relation to the second night value by band for the He I emission line. Errors are also included.

The data assembled in Table 4.15 as well as the information shown in Figure 4.16, allow us to conclude that, regarding the blue band, the third and first night fluxes present the higher variability, respectively. Remarkably, the last night flux presents a low variability. Regarding the red band, we decided just to take into account the absorption area in the wing. The third night is the one which shows a higher variability, as can be seen in Figure 4.16, despite the value of the equivalent width is the lowest. This is caused because the absorption and emission areas have equivalent width values with distinct sign and they cancel out.

From the data in Tables 4.9, 4.10 and 4.11, we also computed the values of the relative variation for the Paschen lines. Tables 4.16, 4.17 and 4.18 show these values.

Night variation	Blue band	Red band
58383.5 / 58384.5	0.3532 ± 0.2240	0.7913 ± 0.8294
58386.5 / 58384.5	0.4786 ± 0.2381	1.9742 ± 1.1978
58387.5 / 58384.5	0.5041 ± 0.1288	0.8610 ± 0.3148

TABLE 4.16: Equivalent width relative variation in relation to the second night value by band for the Pa 5 emission line. Errors are also included.

Night variation	Blue band	Red band
58383.5 / 58384.5	0.5496 ± 0.3843	6.7497 ± 9.4846
58386.5 / 58384.5	0.8222 ± 0.4279	14.746 ± 25.5197
58387.5 / 58384.5	0.6273 ± 0.1867	5.6101 ± 15.3007

TABLE 4.17: Equivalent width relative variation in relation to the second night value by band for the Pa 6 emission line. Errors are also included.

Night variation	Blue band	Red band
58383.5 / 58384.5	0.1967 ± 0.4293	13.7248 ± 155.1146
58386.5 / 58384.5	0.8552 ± 0.5699	55.2085 ± 564.4295
58387.5 / 58384.5	0.9911 ± 0.1755	24.8537 ± 225.5345

TABLE 4.18: Equivalent width relative variation in relation to the second night value by band for the Pa 7 emission line. Errors are also included.

Regarding the blue band, for both Pa 5 and Pa 7 lines, the last night of observation flux values present the highest variability in relation to the second night's, whereas the first night values are the least variable for the three lines. For Pa 6, the third night shows the maximum variability. Moreover, Pa 5 variability is, in general, lower than the other two Paschen lines regarding this blue band. With regard to Pa 7 line, the variability among the observation nights, in terms of equivalent width, is higher and increases as the nights go by.

As regards the red band, also the three emission lines present the same behaviour. As the observation nights go by, the variability regarding the second night flux increases and then, decreases in the last night, as can be seen in Figures 4.18I, 4.18II and 4.18III and in Tables 4.16, 4.17 and 4.18.

To sum up this part, we can say that the last night of observation is the one with a higher variability in relation to the second one and, the more fluctuating activity appears in the red wing of the line profile. This result suggest we are probably witnessing a variation of the mass accretion rate along the accretion columns.

And now, as before, we computed the variation of the equivalent width in respect to the second night value for Br 7 line. These values are gathered in Table 4.19.

Night variation	Blue band	Red band
58383.5 / 58384.5	0.1120 ± 0.3555	0.4814 ± 1.6240
58386.5 / 58384.5	0.1786 ± 0.3680	1.2454 ± 2.1363
58387.5 / 58384.5	0.3207 ± 0.2745	0.5269 ± 0.9479

TABLE 4.19: Equivalent width relative variation in relation to the second night value by band for the Br 7 emission line. Errors are also included.

According to Table 4.19 and Figure 4.18IV, it is easy to check that there does not exist a big variability regarding this emission line. In the blue band, the variability is minimal, although the last night of observation flux diverts a little. In relation to the red band, we can see a higher variability, highlighting the third night.

4.4 Absorption components quantification

In this section, we shall perform a Gaussian fitting to the emission lines which have been addressed in the previous sections. Fitting the emission lines using one or several Gaussian functions will allow us to quantify and compare the absorption between different lines. Moreover, this fitting will also allow us to study the dynamics of the star-disk system, in other words, the chosen parameters for the Gaussian fitting will give us an idea of the accretion velocities and mass. Even so, this is a work still in progress and the results presented here should be considered as preliminary.

4.4.1 Fitting procedure

Now, we shall present the methods which were used to obtain the Gaussian fitting. We will use double or triple Gaussian functions. So, we defined the following function G, such that

$$G(x; a_i, x_{0,i}, \sigma_i) = \sum_i a_i \exp\left[-\frac{(x - x_{0,i})^2}{2\sigma_i^2}\right], \tag{4.6}$$

where $x_{0,i}$ represents the position of the centre of the peak, a_i the height of the Gaussian peak and σ_i the standard deviation. Let's note that the i index indicates the components of the Gaussian function. We will work with $i = 2$ (one emission and one absorption components) for the NIR and Na I D_2 lines and with $i = 3$ (one emission and two absorption components) for the Hα line. In other words, we will use a double Gaussian

function for all lines except from Hα, for which we shall use a triple Gaussian. This is due to the necessity of fitting both blue and red absorption components in Hα line, whereas it is enough only one absorption component for the rest of the emission lines. This kind of fitting presents a huge number of solutions and lots of them have no physical meaning. Consequently, it is necessary to introduce some constraints in one or multiple of the components so as to obtain meaningful results.

First, as examples, we will show the double Gaussian fitting for the He I line and the triple one for Hα line. In Appendix A, we include the fitting results for the rest of the lines. We have to choose the initial parameters for both cases. We did notice that in the case of emission lines, the velocity wings remain constant in each line. We select the line with the highest intensity and fit only the line wings with a Gaussian (which correspond to the third night of observation (MJD: 58386.5)). We established the parameters for the emission component and the fitting produced the following results for the He I line (rounded to the hundredths): $x_{0,1} = 22.31$ km s^{-1}, $a_1 = 1.50$, $\sigma_1 = 123.15$ km s^{-1}, $x_{0,2} = 40.74$ km s^{-1}, $a_2 = -1.85$ and $\sigma_2 = 80.12$ km s^{-1} (the units of intensity are arbitrary since they depend on the continuum normalisation of the line). So, we set the initial parameters to $p_0 = (x_{0,1} = 22.00 \text{ km s}^{-1}, a_1 = 1.50, \sigma_1 = 123.00 \text{ km s}^{-1}, x_{0,2} = 110.00 \text{ km s}^{-1}, a_2 = -1.00, \sigma_2 = 50.00 \text{ km s}^{-1})$ and, as a restriction, we kept constant the parameters for the first or emission component to $x_{0,1} = 22.00$ km s^{-1}, $a_1 = 1.50$ and $\sigma_1 = 123.00$ km s^{-1} for the rest of the nights. Table 4.20 shows the obtained values as well as the computed equivalent width for each Gaussian and Figure 4.21 gathers all nights fittings. Physically, the emission and absorption components of the He I fitting can be associated with different regions. The emission component is centered close to the stellar rest frame and is associated to accretion columns near the stellar surface where the shock occurs and the matter decrease its velocity. The redshifted absorption is due to the opacity of the matter in accretion to the star that block the emission of the region near the star, and the velocity is the average velocity of matter before reaching the stellar surface.

Parameters / Night MJD	58383.5	58384.5	58386.5	58387.5
$x_{0,1}$	22.00	22.00	22.31	22.00
a_1	1.50	1.50	1.50	1.50
σ_1	123.00	123.00	123.15	123.00
W_1	-16.70	-16.70	-16.77	-16.70
$x_{0,2}$	48.18	31.94	40.74	33.02
a_2	-1.80	-1.71	-1.85	-1.87
σ_2	92.49	114.35	80.12	108.79
W_2	15.07	17.69	13.45	18.45

TABLE 4.20: Parameters for the He I double Gaussian fitting. Parameters x and σ are expressed in km s^{-1}, a in arbitrary units and W in Å.

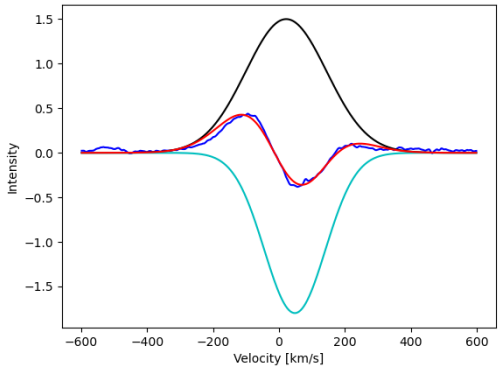

(I) MJD: 58383.5.

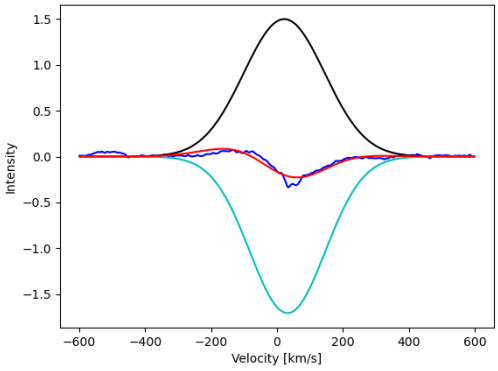

(II) MJD: 58384.5.

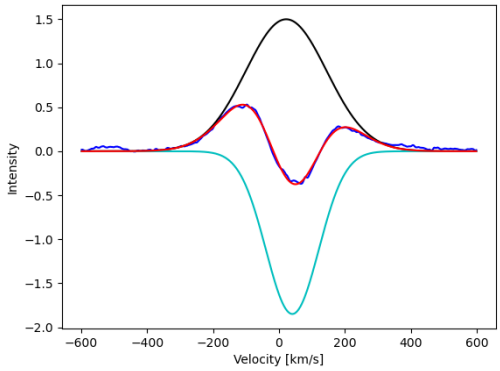

(III) MJD: 58386.5.

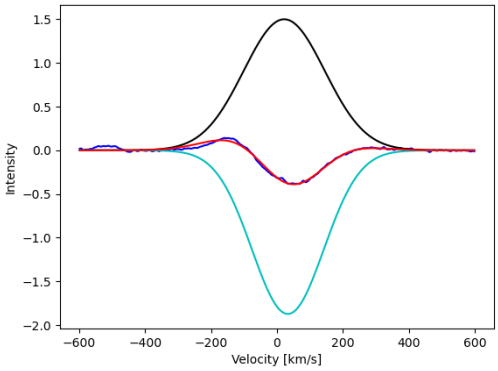

(IV) MJD: 58387.5.

FIGURE 4.21: He I double Gaussian fitting. The black curve corresponds to the first Gaussian component (emission), the light blue curve to the second Gaussian component (absorption) and the red curve to the double Gaussian fitting.

For the Hα case, we adopted a similar procedure. In this particular case we notice that the wings of the emission lines are stable from night to night, as can be seen in Figure 4.14, and so we chose the initial parameters to fit the average wings of the emission component of the line. We fixed the height of the Gaussian and the standard

deviation to $a_1 = 4.00$ and $\sigma_1 = 115.00$ km s^{-1} for all nights. The initial parameters were taken as follows (rounded to the hundredths): $p_0 = (x_{0,1} = 20.00 \text{ km s}^{-1}, a_1 = 4.00, \sigma_1 = 115.00 \text{ km s}^{-1}, x_{0,2} = 50.00 \text{ km s}^{-1}, a_2 = -1.00, \sigma_2 = 50.00 \text{ km s}^{-1}, x_{0,3} = -50.00 \text{ km s}^{-1}, a_3 = -1.00, \sigma_3 = 50.00 \text{ km s}^{-1})$. The standard deviation of the second component was imposed to be less or equal to 70.00 km s^{-1} in order to guarantee a meaningful blueshifted absorption. Table 4.21 shows the obtained values for all nights, accompanied by the equivalent width values for each Gaussian too. Figure 4.22 shows the resulting fittings for all nights. The sources of Hα line are diverse because the line can be emitted in different conditions of temperatures and densities. So we expect emission in Hα from accretion and outflow regions and in large regions surrounding the star. Though presumably optically thick, the fittings show us that we need two components of absorption to get the profile observed. The redshifted absorption component seems to be related to the NIR absorption component and associated to the mass accretion into the star. Furthermore, the blueshifted absorption component is only present in this line and should be caused by a micro-jet present in RY Tau star which has already been reported (St-Onge and Bastien [2008], Agra-Amboage et al. [2009]).

Parameters / Night MJD	58384.9	58386.9	58387.8	58388.8
$x_{0,1}$	21.77	6.02	9.67	16.85
a_1	4.00	4.00	4.00	4.00
σ_1	115.00	115.00	115.00	115.00
W_3	-25.23	-25.23	-25.23	-25.23
$x_{0,2}$	73.72	52.92	50.01	47.22
a_2	-2.28	-2.26	-2.26	-2.89
σ_2	70.00	63.58	70.00	70.00
W_2	8.77	7.89	8.69	11.09
$x_{0,3}$	-40.56	-55.35	-65.55	-57.52
$a3$	-2.24	-2.40	-2.18	-1.77
σ_3	56.66	59.60	57.44	47.04
W_3	6.96	7.86	6.87	4.57

TABLE 4.21: Parameters for the Hα triple Gaussian fitting. Parameters x and σ are expressed in km s^{-1}, a in arbitrary units and W in Å.

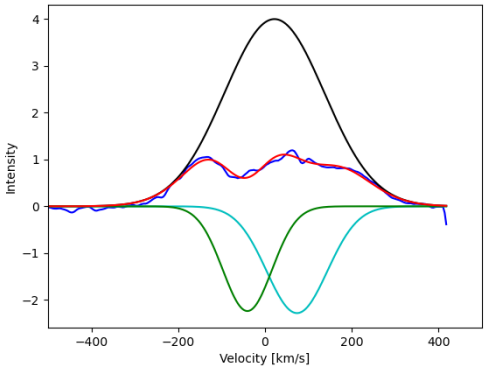

(I) MJD: 58384.9.

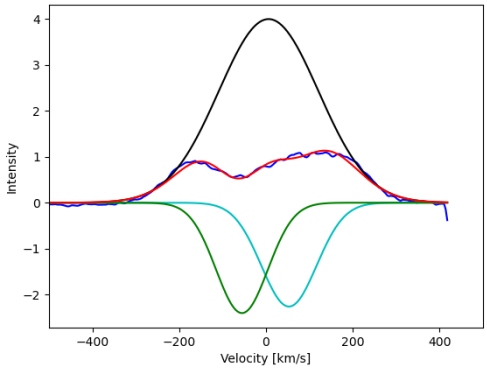

(II) MJD: 58386.9.

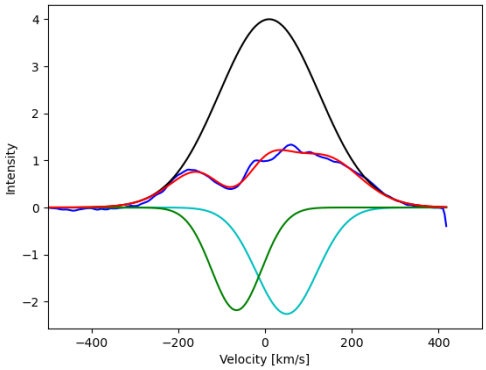

(III) MJD: 58387.8.

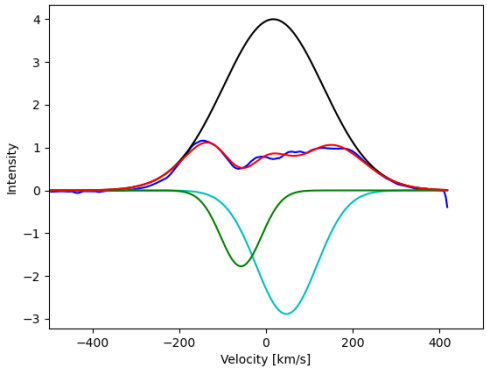

(IV) MJD: 58388.8.

FIGURE 4.22: Hα triple Gaussian fitting. The black curve corresponds to the first Gaussian component (emission), the light blue curve to the second Gaussian component (redshifted absorption), the green curve to the third Gaussian component (blueshifted absorption) and the red curve to the triple Gaussian fitting.

4.4.2 Comparative analysis between lines

In this subsection, we will address an analysis so as to compare the absorption between the different lines which we have introduce in the previous sections.

Let's start with the NIR lines. Regarding Paschen ones, it is expected that the components of the fitting will be similar, since these lines originate closely, in the same region, specifically in the accretion columns. Brackett and He I lines are expected to present a slightly different behaviour in respect to Paschen lines and between themselves, since these two lines are originated in distinct but also close areas.

In Figure 4.23, we show the equivalent width variation of the second or absorption component of the fitting for Paschen, Brackett, He I and Na I D_2 lines. Indeed, we can observe the same general behaviour for all the cited lines. Let's note that, just as we concluded in the previous sections, the maximum absorption occurs in the MJD: 58387.5

night, which corresponds with the last night for the NIR observations and the third one for the optical.

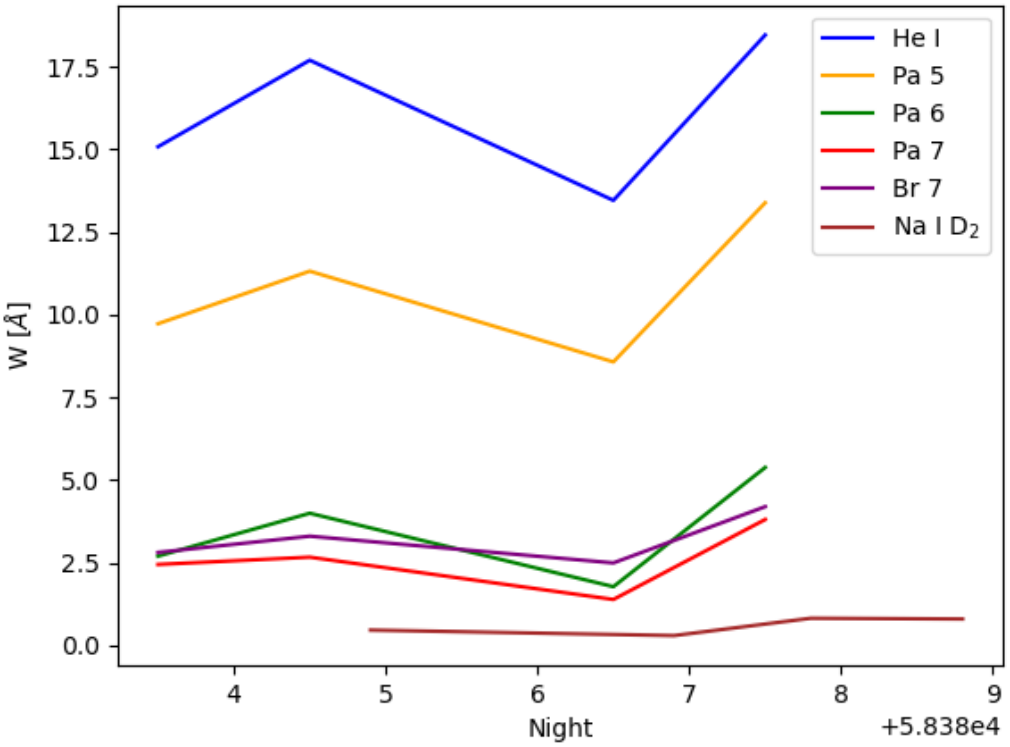

FIGURE 4.23: Evolution of the equivalent width value of the second or absorption component of the fitting for He I, Paschen, Brackett and Na I D_2 lines.

Regarding Hα line, it is obvious the need of a third absorption component to fit the profile shape. A good fitting can be achieved with a strong emission Gaussian and two absorption in both red and blue wings. However, we have found that the final fitting depends on the initial parameters guess and constraints adopted. To illustrate this situation, two scenarios are presented in Figure 4.24. The first case, shown in Figure 4.24I, represents the solution obtained in Figure 4.22 and Table 4.21. The Hα redshifted absorption component correlates with the absorption component in the NIR lines (and in particular the He I line) and anticorrelates with the blueshifted absorption. This behaviour is not in agreement with the results found through the equivalent widths analysis. Nevertheless, if we impose new constraints on the redshifted absorption component, these results are different. It is important to underline that these fittings are highly dependent on the chosen parameters and constraints. Figure 4.24II shows the equivalent width values of the blueshifted absorption component after imposing the redshifted component standard

deviation to be equal to $\sigma_2 = 66.00$ km s^{-1}. In this case, it is possible to see that the maximum in the blueshifted absorption for Hα happens after the maximum of the redshifted absorption for the He I line, supporting the fact of outflow being directly related to accretion. Let's note that the behaviour of the redshifted absorption component of Hα is opposed to the blueshifted components', as expected.

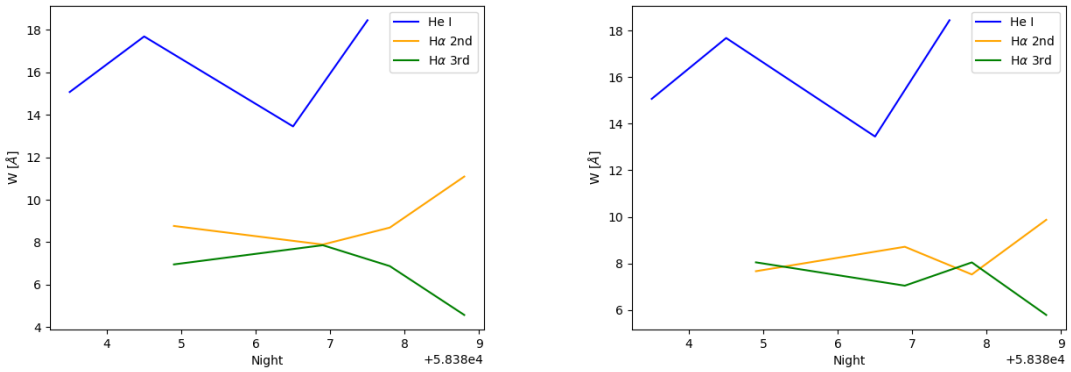

(I) First scenario corresponding to the fitting addressed in Section 4.4.1.

(II) Second scenario corresponding to the new fitting after having imposed $\sigma_2 = 66.00$ km s^{-1} for Hα.

FIGURE 4.24: Evolution of the equivalent width value of the second component of the fitting for He I and Hα, together with the evolution of the equivalent width value of the third component of the fitting for Hα.

Chapter 5

Conclusions

This Master's degree dissertation has conducted a path which began with an approach to a specific kind of low-mass stars called T Tauri stars, concentrating on their formation process as well as presenting their subtypes, focusing on Classical T Tauri stars. This sort of objects are characterised by possessing a circumstellar disk and presenting a strong interaction between both stellar and disk structures through the stellar magnetic field.

This interaction consists of accretion and outflow processes, in fact, it can be defined as an equilibrium between them, moreover, outflow is thought to be directly related to accretion. This connection is one of the issues that has been addressed in this dissertation and it will be related afterwards. The main accretion models were also discussed in this text. We presented the standard or classical model and its defects, as well as the current magnetospheric model. Regarding outflow, we described the principal phenomena such as stellar, disk, conical, and X-winds, magnetospheric ejections and jets along with their main causes and consequences.

Later on, we started to focus on our particular case. The SPIRou spectropolarimeter and velocimeter was introduced together with the SPIRou Legacy Survey. Their main characteristics and objectives were also addressed, specifically, the SPIRou data reduction was explained so as to understand the data we were going to handle. We also presented the main characteristics of our target star in this work, RY Tau.

Finally, in the fourth chapter, we addressed the practical task with the SPIRou data of RY Tau. We worked with NIR and optical observations from few nights observed in September 2018. Our objective was to study some lines, namely Paschen (Pa 5, Pa 6 and Pa 7), Bracket (Br 7) and Helium (He I) in the NIR and Hα and sodium (Na I D) in the optical, so as to analyse the accretion and outflow phenomena linked to absorption and

emission in these lines. This is part of the aforementioned objective of finding a relation between accretion and outflow processes.

Firstly, we introduced the data treatment which was necessary to perform so as to obtain interpretable results, that is, a residual spectrum that allows us to observe the intrinsic variations of the lines by removing the photospheric absorptions. A residual spectrum is obtained, in our case, by subtracting a simulated spectrum to the observed one. So as to do so, we got a simulated spectrum from BT-Settl synthetic grid spectra by performing the rotational and instrumental broadening. Before the subtraction, we also shifted the observed spectra to get the photospheric lines in the stellar rest frame, we applied a noise filtering to obtain a cleaner flux and, finally, we normalised the spectra to the continuum.

Then, we analysed the variability of the residual spectra of the aforementioned emission lines. Concerning the optical lines, Hα shows a blueshifted absorption which is an evidence of outflow phenomena like stellar, disk or conical winds. Na I D_2 line shows redshifted absorption, meaning the presence of infalling gas in the observer line of sight. Then, regarding the NIR lines, He I provides us with some interesting information. The observable inverse P Cygni profile indicates a considerable amount of mass in accretion and its velocity stability induces us to think that there does not exist strong variations of the magnetic topology during the observations. Paschen lines behave similarly among them. The spectrum corresponding to the last night of observation (MJD: 58387.5) also presents an inverse P Cygni profile, suggesting a growth of the accretion mass during this night. Brackett line shows a behaviour analogous to Paschen's, absorption is less intense in general and increases on the last night. In summary, the NIR and Na I D_2 lines present profile variations in the red wing, indicating strong and variable accretion processes. Furthermore, Hα line shows its profile variations in the blue wing, tracing the stellar outflow activity.

After, we dealt with the equivalent width analysis of the emission lines. This study allowed us to quantify the variability of the lines as well as to investigate the relation between accretion and outflow. We calculated the value of the equivalent width along to its error for all the lines, during all the nights and by bands, defining a blue, red and full band for each line. Paschen and Brackett equivalent widths behave in the same way. There exists an increase of the equivalent width value from the first to the second night, then a decrease to the third night and, finally, a new increase to the last night. This analogous behaviour was expectable since the four lines are originated in close regions. Concerning

He I line, the behaviour of the equivalent width values is the same. Finally, in relation to optical lines, the line which presents a distinct behaviour is Hα. When the NIR and Na D lines present the main variability in the red wing, the Hα shows both variations in the blue and red wings. If the redshifted absorption is related to the absorption on the other lines, we search for anticorrelation with the blueshifted absorption. We also computed the relative variation of the equivalent width values with respect to a reference night in order to quantify and compare variations between different lines and bands. Though the information provided by this relative variation supports our previous conclusions, the low level of intensity in few lines does not allow us to draw further conclusions.

To finish, we carried out a quantification of the absorption components by fitting the analysed emission lines with Gaussian functions. We used two Gaussian functions (an emission and an absorption components) for the NIR and the Na I D_2 lines, whereas we used three Gaussian functions (an emission and two absorption components) for the Hα line. These fittings admit multiple solutions and are really highly dependent on the initial parameters and the imposed constraints, so we had to carefully choose the constraints so that the fitting made physical sense. The obtained results are still preliminary and may be improved in the future. For now and under some specific constraints, results are consistent with the equivalent width analysis. The main result is that the behaviour of the blueshifted absorption in Hα line is related with the redshifted absorption observed in all the lines. The results strongly suggest that the outflow is a consequence of the mass accretion into the star.

To conclude, the work done in this dissertation provides evidence that it is possible to observe the direct relation between interaction processes, such as accretion and outflow, in star-disk systems. The case treated in this project shows, for the first time, the connection between accretion and outflow. All the programs developed in Python for the treatment and analysis of the data can be used to further investigate new data in this or other Classical T Tauri stars provided by SPIRou.

Appendix A

Absorption components quantification fitting results

In this appendix, we include the results generated by the fitting for the emission lines which were not included in the analysis of Section 4.4. Let's remind that these are provisional results and they are highly dependent on the chosen initial parameters and constraints. We include the results for Pa 5 (Table A.1), Pa 6 (Table A.2), Pa 7 (Table A.3), Br 7 (Table A.4) and Na I D_2 (Table A.5) lines. The units and initial parameters are indicated in the captions. Let's remind that Figure 4.23 shows the equivalent width values of the second component (W_2) for the following fittings, together with the values relating to He I line.

Parameters / Night MJD	58383.5	58384.5	58386.5	58387.5
$x_{0,1}$	0.00	0.00	0.0	0.00
a_1	1.34	1.34	1.34	1.34
σ_1	101.00	101.00	101.21	101.00
W_1	-14.49	-14.49	-14.49	-14.49
$x_{0,2}$	15.96	14.23	10.70	11.15
a_2	-1.06	-1.13	-1.04	-1.37
σ_2	85.56	93.06	77.40	91.00
W_2	9.72	11.31	8.57	13.38

TABLE A.1: Parameters for the Pa 5 double Gaussian fitting. Parameters x and σ are expressed in km s^{-1}, a in arbitrary units and W in Å. The initial parameters are $p_0 = (x_{0,1} = 0.00 \text{ km s}^{-1}, a_1 = 1.34, \sigma_1 = 101.00 \text{ km s}^{-1}, x_{0,2} = 110.00 \text{ km s}^{-1}, a_2 = -1.00, \sigma_2 = 50.00 \text{ km s}^{-1}$.

Parameters / Night MJD	58383.5	58384.5	58386.5	58387.5
$x_{0,1}$	-6.00	-6.00	-5.85	-6.00
a_1	0.50	0.50	0.50	0.50
σ_1	110.00	110.00	109.80	110.00
W_1	-5.03	-5.03	-5.02	-5.03
$x_{0,2}$	36.88	32.08	25.94	23.69
a_2	-0.36	-0.46	-0.31	-0.68
σ_2	82.82	94.67	63.38	86.48
W_2	2.70	4.00	1.78	5.38

TABLE A.2: Parameters for the Pa 6 double Gaussian fitting. Parameters x and σ are expressed in km s^{-1}, a in arbitrary units and W in Å. The initial parameters are $p_0 = (x_{0,1} = -6.00 \text{ km s}^{-1}, a_1 = 0.50, \sigma_1 = 110.00 \text{ km s}^{-1}, x_{0,2} = 110.00 \text{ km s}^{-1}, a_2 = -1.00, \sigma_2 = 50.00 \text{ km s}^{-1}$.

Parameters / Night MJD	58383.5	58384.5	58386.5	58387.5
$x_{0,1}$	-19.00	-19.00	-19.01	-19.00
a_1	0.40	0.40	0.41	0.40
σ_1	100.00	100.00	99.99	100.00
W_1	-3.36	-3.36	-3.44	-3.36
$x_{0,2}$	6.21	9.59	0.00	1.11
a_2	-0.30	-0.35	-0.23	-0.55
σ_2	98.17	90.11	71.10	82.86
W_2	2.45	2.69	1.39	3.81

TABLE A.3: Parameters for the Pa 7 double Gaussian fitting. Parameters x and σ are expressed in km s^{-1}, a in arbitrary units and W in Å. The initial parameters are $p_0 = (x_{0,1} = -19.00 \text{ km s}^{-1}, a_1 = 0.40, \sigma_1 = 100.00 \text{ km s}^{-1}, x_{0,2} = 110.00 \text{ km s}^{-1}, a_2 = -1.00, \sigma_2 = 50.00 \text{ km s}^{-1}$.

Parameters / Night MJD	58383.5	58384.5	58386.5	58387.5
$x_{0,1}$	19.00	19.00	19.49	19.00
a_1	0.39	0.39	0.39	0.39
σ_1	73.00	73.00	72.64	73.00
W_1	-5.15	-5.15	-5.15	-5.15
$x_{0,2}$	46.66	49.47	42.71	46.07
a_2	-0.26	-0.30	-0.25	-0.37
σ_2	58.89	60.26	54.13	63.44
W_2	2.81	3.30	2.49	4.20

TABLE A.4: Parameters for the Br 7 double Gaussian fitting. Parameters x and σ are expressed in km s^{-1}, a in arbitrary units and W in Å. The initial parameters are $p_0 = (x_{0,1} = 19.00 \text{ km s}^{-1}, a_1 = 0.39, \sigma_1 = 73.00 \text{ km s}^{-1}, x_{0,2} = 110.00 \text{ km s}^{-1}, a_2 = -1.00, \sigma_2 = 50.00 \text{ km s}^{-1}$.

Parameters / Night MJD	58384.9	58386.9	58387.8	58388.8
$x_{0,1}$	4.41	9.98	5.32	12.35
a_1	-0.25	0.27	-0.19	-0.21
σ_1	8.10	7.92	7.43	7.85
W_1	0.10	0.11	0.07	0.08
$x_{0,2}$	28.19	32.06	31.60	37.97
a_2	-0.21	-0.18	-0.33	-0.44
σ_2	44.95	33.14	51.28	36.59
W_2	0.46	0.30	0.82	0.80

TABLE A.5: Parameters for the Na I D_2 double Gaussian fitting. Parameters x and σ are expressed in km s^{-1}, a in arbitrary units and W in Å.

Bibliography

F. C. Adams, F. C. Lada, and F. H. Shu. Spectral Evolution of Young Stellar Objects. The Astrophysical Journal, 312:788–806, jan 1987. URL http://articles.adsabs.harvard.edu/pdf/1987ApJ...312..788A. [Cited on page 7.]

V. Agra-Amboage, C. Dougados, S. Cabrit, P. J. V. García, and P. Ferruit. [O I] sub-arcsecond study of a microjet from an intermediate mass young star: RY Tauri. Astronomy and Astrophysics, 493:1029–1041, 2009. URL https://www.aanda.org/articles/aa/pdf/2009/03/aa10025-08.pdf. [Cited on page 54.]

J. M. Alcalá, A. Natta, C. F. Manara, L. Spezzi, B. Stelzer, A. Frasca, K. Biazzo, E. Covino, S. Randich, E. Rigliaco, L. Testi, F Comerón, G. Cupani, and V. D'Elia. X-shooter spectroscopy of young stellar objects. IV. Accretion in low-mass stars and substellar objects in Lupus. Astronomy & Astrophysics, 561 - A2, 2014. URL https://www.aanda.org/articles/aa/pdf/2014/01/aa22254-13.pdf. [Cited on page 24.]

P. André. in The Cold Universe. 1994. [Cited on pages xiii and 7.]

M. Barsony. Class 0 Protostars. Astronomical Society of the Pacific Conference Series, 65:197–206, 1994. URL http://articles.adsabs.harvard.edu/pdf/1994ASPC...65..197B. [Cited on page 7.]

G. Basri, G. W. Marcy, and J. A. Valenti. Limits on the Magnetic Flux of Pre-Main-Sequence Stars. The Astrophysical Journal, 390:622–633, 1992. URL http://articles.adsabs.harvard.edu/pdf/1992ApJ...390..622B. [Cited on page 10.]

S. Beckwith, J. Staude, A. Quetz, and A. Natta, editors. Disks and Outflows Around Young Stars. Springer Berlin Heidelberg, 1996. [Cited on page 16.]

C. Bertout. T Tauri Stars: Wild as Dust. Annual Review of Astronomy and Astrophysics, 27:351–395, 1989. URL http://articles.adsabs.harvard.edu/pdf/1989ARA%26A..27..351B. [Cited on pages xiii and 4.]

J. Bouvier, S. H. P. Alencar, T. Boutelier, C. Dougados, Z. Balog, K. Grankin, S. T. Hodgkin, M. A. Ibrahimov, M. Kun, T. Y. Magakian, and C. Pinte. Magnetospheric accretion-ejection processes in the classical T Tauri star AA Tauri. Astronomy & Astrophysics, 463: 1017–1028, 2006. URL https://www.aanda.org/articles/aa/pdf/2007/09/aa6021-06.pdf. [Cited on page 11.]

J. Bouvier, S. P. Matt, S. Mohanty, A. Scholz, K. G. Stassun, and C. Zanni. Angular momentum evolution of young low-mass stars and brown dwarfs: observations and theory. Protostars and Planets, IV:433–450, 2014. URL https://arxiv.org/pdf/1309.7851.pdf. [Cited on pages xiii and 14.]

F. S. Brackett. Visible and Infra-Red Radiation of Hydrogen. The Astrophysical Journal, 56: 154–161, 1922. URL http://cdsads.u-strasbg.fr/pdf/1922ApJ....56..154B. [Cited on page 24.]

S. Cabrit. The accretion-ejection connexion in T Tauri stars: jet models vs. observations. IAU Symposium, 243:203–214, 2007. URL http://articles.adsabs.harvard.edu/pdf/2007IAUS..243..203C. [Cited on pages 9 and 13.]

B. W. Carroll and D. A. Ostlie. An Introduction to Modern Astrophysics. Cambridge University Press, 2017. [Cited on page 38.]

R. Cloutier, E. Artigau, X. Delfosse, L. Malo, C. Moutou, R. Doyon, J. F. Donati, A. Cumming, X. Dumusque, E. Hébrard, and K. Menou. Predictions of planet detections with near infrared radial velocities in the up-coming SPIRou Legacy Survey-Planet Search. The Astrophysical Journal, 155, 2017. URL https://arxiv.org/pdf/1712.06673.pdf. [Cited on page 17.]

G. W. Collins. The Fundamentals of Stellar Astrophysics. 1989. [Cited on pages xiii and 2.]

C. L. Davies, S. Kraus, T. J. Harries, J. D. Monnier, B. Kloppenborg, A. Aarnio, F. Baron, R. Garcia, R. Millan-Gabet, R. Parks, E. Pedretti, K. Perraut, J. Sturmann, L. Sturmann, T. A. ten Brummelaar, and Y. Touhami. The inner disk of RY Tau: evidence of stellar occultation by the disk atmosphere at the sublimation rim from K-band continuum

interferometry. The Astrophysical Journal, 897, 2020. URL https://arxiv.org/pdf/2005.06932.pdf. [Cited on page 22.]

R. M. G. de Albuquerque. Diagnostic line profiles and modelling of the accretion and outflow regions around YSOs. Master's thesis, University of Porto, 2015. [Cited on pages 3, 5, and 10.]

R. M. G. de Albuquerque. Accretion versus outflow regions around Young Stellar Objects. PhD thesis, University of Porto, 2019. [Cited on pages 3 and 11.]

R. M. G. de Albuquerque, J. F. Gameiro, S. H. P. Alencar, J. J. G. Lima, C. Sauty, and C. Melo. Accretion in low-mass members of the Orion Nebula Cluster with young transition disks. Astronomy & Astrophysics, 636 - A86, 2020. URL https://www.aanda.org/articles/aa/pdf/2020/04/aa36694-19.pdf. [Cited on page 38.]

S. Edwards, W. Fischer, L. Hillenbrand, and J. Kwan. Probing T Tauri Accretion and Outflow with 1 Micron Spectroscopy. The Astrophysical Journal, 646:319–341, 2006. URL https://iopscience.iop.org/article/10.1086/504832/pdf. [Cited on pages 33 and 37.]

C. Eiroa, R. D. Oudmaijer, J. K. Davies, D. de Winter, F. Garzón, J. Palacios, A. Alberdi, R. Ferlet, C. A. Grady, A. Cameron, H. J. Deeg, A. W. Harris, K. Horne, B. Merlín, L. F. Miranda, B. Montesinos, A. Mora, A. Penny, A. Quirrenbach, H. Rauer, J. Schneider, E. Solano, Y. Tsapras, and P. R. Wesselius. On the simultaneous optical and near-infrared variability of pre-main sequence stars. Astronomy & Astrophysics, 384:1038–1049, 2002. URL https://www.aanda.org/articles/aa/pdf/2002/12/aa2139.pdf. [Cited on page 20.]

B. Ercolano and I. Pascucci. The Dispersal of Planet-forming discs: Theory confronts Observations. Royal Society Open Science, 4, 2017. URL https://arxiv.org/pdf/1704.00214.pdf. [Cited on pages 6 and 7.]

J. Ferreira. Braking down an accreting protostar: disc-locking, disc winds, stellar winds, X-winds and Magnetospheric Ejecta. EAS Publication Series, 62:169–225, 2013. URL https://arxiv.org/pdf/1310.4203.pdf. [Cited on page 13.]

A. Frank, T. P. Ray, S. Cabrit, P. Hartigan, H. G. Arce, F. Bacciotti, J. Bally, M. Benisty, J. Eislöffel, M. Güdel, S. Lebedev, B. Nisini, and A. Raga. Jets and Outflows From Star

to Cloud: Observations Confront Theory. Protostars and Planets, VI:451–474, 2014. URL https://arxiv.org/pdf/1402.3553.pdf. [Cited on pages xiii and 16.]

F. Gallet and J. Bouvier. Improved angular momentum evolution model for solar-like stars. Astronomy & Astrophysics, 556(A36), 2013. URL https://www.aanda.org/articles/aa/pdf/2013/08/aa21302-13.pdf. [Cited on page 7.]

P. Ghosh and F. K. Lamb. Accretion by rotating magnetic neutron stars. II. Radial and vertical structure of the transition zone in disk accretion. The Astrophysical Journal, 232: 259–276, 1979. URL http://cdsads.u-strasbg.fr/pdf/1979ApJ...232..259G. [Cited on page 15.]

U. Gorti, R. Liseau, Z. Sándor, and C. Clarke. Disk Dispersal: Theoretical Understanding and Observational Constraints. Space Science Reviews, 205:125–152, 2016. URL https://arxiv.org/pdf/1512.04622.pdf. [Cited on page 7.]

D. F. Gray. The Observation and Analysis of Stellar Photospheres. Cambridge University Press, 2005. [Cited on page 28.]

M. Güdel, K. R. Briggs, K. Arzner, M. Audard, J. Bouvier, E. D. Feigelson, E. Franciosini, A. Glauser, N. Grosso, G. Micela, J. L. Monin, T. Montmerle, D. L. Padgett, F. Palla, I. Pillitteri, L. Rebull, L. Scelsi, B. Silva, S. L. Skinner, B. Stelzer, and A. Telleschi. The XMM-Newton extended survey of the Taurus molecular cloud (XEST). Astronomy & Astrophysics, 468:353–377, 2006. URL https://www.aanda.org/articles/aa/pdf/2007/23/aa5724-06.pdf. [Cited on page 22.]

P. Hartigan, S. Edwards, and L. Ghandour. Disk Accretion and Mass Loss from Young Stars. The Astrophysical Journal, 452:736–768, 1995. URL http://articles.adsabs.harvard.edu/pdf/1995ApJ...452..736H. [Cited on page 9.]

L. Hartmann. Accretion Processes in Star Formation. Cambridge University Press, 2008. [Cited on page 12.]

L. Hartmann, R. Hewett, and N. Calvet. Magnetospheric accretion models for T Tauri stars. 1: Balmer line profiles without rotation. The Astrophysical Journal, 426:669–687, 1994. URL http://articles.adsabs.harvard.edu/pdf/1994ApJ...426..669H. [Cited on page 37.]

L. Hartmann, G. Herczeg, and N. Calvet. Accretion onto Pre-Main-Sequence Stars. Annual Review of Astronomy and Astrophysics, 54:135–180, 2016. URL https://www2.mpia-hd.mpg.de/~beuther/hartmann2016.pdf. [Cited on pages xiii and 6.]

C. Hayashi. Stellar evolution in early phases of gravitational contraction. Publications of the Astronomical Society of Japan, 13:450–452, 1961. URL http://articles.adsabs.harvard.edu/pdf/1961PASJ...13..450H. [Cited on page 2.]

L. G. Henyey, R. Lelevier, and R. D. Levée. The Early Phases of Stellar Evolution. Publications of the Astronomical Society of the Pacific, 67:154–160, 1955. URL https://iopscience.iop.org/article/10.1086/126791/pdf. [Cited on page 2.]

W. Herbst and P. C. Stine. Photometric variations of Orion population stars. III - RY Tau, T Ori, NV Ori, and HH AUR. The Astronomical Journal, 89:1716–1720, 1984. URL http://articles.adsabs.harvard.edu/pdf/1984AJ.....89.1716H. [Cited on page 21.]

W. Herbst, D. K. Herbst, E. J. Grossman, and D. Weinstein. Catalogue of UBVRI Photometry of T Tauri Stars and Analysis of the Causes of Their Variability. The Astronomical Journal, 108:1906–1923, 1994. URL http://articles.adsabs.harvard.edu/pdf/1994AJ....108.1906H. [Cited on page 21.]

J. Hernández, L. Hartmann, N. Calvet, R. D. Jeffries, R. Gutermuth, J. Muzerolle, and J. Stauffer. A Spitzer View of Protoplanetary Disks in the γ Velorum Cluster. The Astrophysical Journal, 686:1195–1208, 2008. URL https://arxiv.org/pdf/0806.2639.pdf. [Cited on page 7.]

J. Kwan, S. Edwards, and W. Fischer. Modeling T Tauri Winds from He I λ10830 Profiles. The Astrophysical Journal, 657:897–915, 2007. URL https://iopscience.iop.org/article/10.1086/511057/pdf. [Cited on pages 33 and 37.]

C. Lada and B. A. Wilking. The nature of the embedded population in the Rho Ophiuchi dark cloud: mid-infrared observations. The Astrophysical Journal, 287:610–621, 1984. URL http://articles.adsabs.harvard.edu/pdf/1984ApJ...287..610L. [Cited on page 7.]

F. Long, G. J. Herczeg, D. Harsono, P. Pinilla, M. Tazzari, C. F. Manara, I. Pascucci, S. Cabrit, B. Nisini, D. Johnstone, S. Edwards, C. Salyk, F. Menard, G. Lodato, Y. Boehler,

G. N. Mace, Y. Liu, G. D. Mulders, N. Hendler, E. Ragusa, W. J. Fischer, A. Banzatti, E. Rigliaco, G. van de Plas, G. Dipierro, M. Gully-Santiago, and R. Lopez-Valdivia. Compact Disks in a High-resolution ALMA Survey of Dust Structures in the Taurus Molecular Cloud. The Astrophysical Journal, 882:49–69, 2019. URL https://iopscience.iop.org/article/10.3847/1538-4357/ab2d2d/pdf. [Cited on page 21.]

D. Lynden-Bell and J. E. Pringle. The evolution of viscous discs and the origin of the nebular variables. Monthly Notices of the Royal Astronomical Society, 168:603–637, 1974. URL http://articles.adsabs.harvard.edu/cgi-bin/nph-iarticle_query?1974MNRAS.168..603L&defaultprint=YES&filetype=.pdf. [Cited on page 9.]

C. F. Manara. The physics of the accretion process in the formation and evolution of Young Stellar Objects. PhD thesis, ESO, 2014. [Cited on page 11.]

S. Matt and R. E. Pudritz. Accretion-Powered Stellar Winds as a Solution to the Stellar Angular Momentum Problem. The Astrophysical Journal, 632:135–138, 2005. URL https://iopscience.iop.org/article/10.1086/498066/pdf. [Cited on page 13.]

M. J. Monteiro. Lecture notes in Stellar Structure and Evolution, 2019. [Cited on page 3.]

C. Moutou, G. Hébrard, E. Hébrard, J. F. Donati, X. Delfosse, D. Kouach, and the SPIRou team. SPIRou: a spectropolarimeter for the CFHT. Proceedings of the Annual meeting of the French Society of Astronomy and Astrophysics, pages 205–212, 2015. URL http://sf2a.eu/proceedings/2015/2015sf2a.conf..0205M.pdf. [Cited on pages xiii, 17, 18, and 19.]

C. Moutou, S. Dalal, J. F. Donati, E. Martioli, C. P. Folsom, É. Artigau, I. Boisse, F. Bouchy, A. Carmona, N. J. Cook, X. Delfosse, R. Doyon, P. Fouqué, G. Gaisné, G. Hébrad, M. Hobson, B. Klein, A. Lecavelier des Etangs, and J. Morin. Early science with SPIRou: near-infrared radial velocity and spectropolarimetry of the planet-hosting star HD 189733. Astronomy & Astrophysics, 642 - A72, 2020. URL https://www.aanda.org/articles/aa/pdf/2020/10/aa38108-20.pdf. [Cited on page 19.]

F. Paschen. Zur Kenntnis ultraroter Linienspektra. I. (Normalwellenlängen bis 27000 Å.-E.). Annalen der Physik, 332(13):537–570, 1908. [Cited on page 24.]

P. P. Petrov. T Tauri Stars. Astrophysics, 46(4):506–529, 2003. URL https://link.springer.com/content/pdf/10.1023/B:ASYS.0000003267.35552.f7.pdf. [Cited on pages 5, 10, and 12.]

P. P. Petrov, G. V. Zajtseva, Yu. S. Efimov, R. Duemmler, I. V. Ilyin, I. Tuominen, and V. A. Shcherbakov. Brightening of the T Tauri star RY Tauri in 1996. Photometry, polarimetry and high-resolution spectroscopy. Astronomy and Astrophysics, 341:553–559, 1999. URL http://articles.adsabs.harvard.edu/pdf/1999A%26A...341..553P. [Cited on pages 20 and 22.]

P. P. Petrov, K. N. Grankin, J. F. Gameiro, S. A. Artemenko, E. V. Babina, R. M. G. de Albuquerque, A. A. Djupvik, G. F. Gahm, V. I. Shenavrin, T. R. Irsmambetova, M. Fernandez, D. E. Mkrtichian, and S. Yu. Gorda. Dynamics of wind and the dusty environments in the accreting T Tauri stars RY Tauri and SU Aurigae. Monthly Notices of the Royal Astronomical Society, 483:132–146, 2019. URL https://arxiv.org/pdf/1811.08635.pdf. [Cited on pages 22, 33, and 38.]

P. P. Petrov, M. M. Romanova, K. N. Grankin, S. A. Artemenko, E. V. Babina, and S. Yu. Gorda. Modulated accretion in the T Tauri star RY Tau - a stable MHD propeller or a planet at 0.2 AU? Monthly Notices of the Royal Astronomical Society, 504:871–877, 2021. URL https://arxiv.org/pdf/2104.00433.pdf. [Cited on pages 23, 24, 33, and 38.]

E. C. Pickering. 71 new variable stars in Harvard Maps Nos. 9, 12, 21, 48 and 51. Astronomische Nachrichten, 175:333–338, 1907. URL http://articles.adsabs.harvard.edu/pdf/1907AN....175..333P. [Cited on page 20.]

B. Reipurth, A. Pedrosa, and M. T. V. T. Lago. Hα emission in pre-main sequence stars. Astronomy & Astrophysics, 120(2):229–256, 1996. URL https://aas.aanda.org/articles/aas/pdf/1996/17/ds1177.pdf. [Cited on pages xiii and 5.]

M. M. Romanova and S. P. Owocki. Accretion, Outflows and Winds of Magnetized Stars. Space Science Reviews, 191:339–389, 2015. URL https://arxiv.org/pdf/1605.04979.pdf. [Cited on pages xiii and 12.]

M. M. Romanova, G. V. Ustyugova, A. V. Koldoba, and R. V. E. Lovelace. Launching of conical winds and axial jets from the disc-magnetosphere boundary: axisymmetric and

3D simulations. Monthly Notices of the Royal Astronomical Society, 399:1802–1828, 2009. URL https://arxiv.org/pdf/0907.3394.pdf. [Cited on page 13.]

M. M. Romanova, G. V. Ustyugova, A. V. Koldoba, and R. V. E. Lovelace. MRI - driven accretion on to magnetized stars: axisymmetric MHD simulations. Monthly Notices of the Royal Astronomical Society, 416:416–438, 2011. URL https://www.researchgate.net/publication/229872194_MRI-driven_accretion_on_to_magnetized_stars_Axisymmetric_MHD_simulations. [Cited on page 15.]

A. A. Schegerer, S. Wolf, Th. Ratzka, and Ch. Leinert. The T Tauri star RY Tauri as a case study of the inner regions of circumstellar dust disks. Astronomy & Astrophysics, 478: 779–793, 2008. URL https://www.aanda.org/articles/aa/pdf/2008/06/aa7049-07.pdf. [Cited on pages 20 and 22.]

N. I. Shakura and R. A. Sunyaev. Black Holes in Binary Systems. Observational Appearance. Astronomy & Astrophysics, 24:337–355, 1973. URL http://articles.adsabs.harvard.edu/cgi-bin/nph-iarticle_query?1973A%26A....24..337S&defaultprint=YES&filetype=.pdf. [Cited on page 9.]

F. H. Shu, F. C. Adams, and S. Lizano. Star formation in molecular clouds: observation and theory. Annual Review of Astronomy and Astrophysics, 25:23–81, 1987. URL http://articles.adsabs.harvard.edu/pdf/1987ARA%26A..25...23S. [Cited on pages xiii and 2.]

G. St-Onge and P. Bastien. A Jet Associated with the Classical T Tauri Star RY Tauri. The Astrophysical Journal, 674:1032–1036, 2008. URL https://iopscience.iop.org/article/10.1086/524649/pdf. [Cited on pages xiii, 21, and 54.]

S. W. Stahler. Understanding Young Stars: A History. Publications of the Astronomical Society of the Pacific, 100:1474–1485, 1988. URL http://articles.adsabs.harvard.edu/pdf/1988PASP..100.1474S. [Cited on pages xiii and 4.]

S. W. Stahler and F. Palla. The Formation of Stars. 2004. [Cited on pages xiii, xiv, 2, 7, 10, 38, and 39.]

M. Takami, J. L. Karr, J. Hashimoto, H. Kim, J. Wisniewski, T Henning, C. A. Grady, R. Kandori, K. W. Hodapp, T. Kudo, N. Kusakabe, M. Y. Chou, Y. Itoh, M. Momose,

S. Mayama, T. Currie, K. B. Follette, J. Kwon, L. Abe, W. Brandner, T. D. Brandt, J. Carson, S. E. Egner, M. Feldt, O. Guyon, Y. Hayano, M. Hayashi, S. Hayashi, M. Ishii, M. Iye, M. Janson, G. R. Knapp, M. Kuzuhara, M. W. McElwain, T. Matsuo, S. Miyama, J. I. Morino, A. Moro-Martin, T. Nishimura, T. S. Pyo, E. Serabyn, H. Suto, E. Suzuki, N. Takato, H. Terada, C. Thalmann, D. Tomono, E. L. Turner, M. Watanabe, T. Yamada, H. Takami, T. Usuda, and M. Tamura. Highcontrast near-infrared imaging polarimetry of the protoplanetary disk around RY TAU. The Astrophysical Journal, 772(145), 2013. [Cited on page 20.]

S. Ulmer-Moll. Atmospheric correction for high-resolution near-infrared spectroscopy. PhD thesis, University of Porto, 2020. [Cited on page 19.]

R. J. White and G. Basri. Very Low Mass Stars and Brown Dwarfs in Taurus-Auriga. The Astrophysical Journal, 582:1109–1122, 2003. URL https://iopscience.iop.org/article/10.1086/344673/pdf. [Cited on page 31.]

J. P. Williams and L. A. Cieza. Protoplanetary Disks and Their Evolution. Annual Review of Astronomy and Astrophysics, 49:67–117, 2011. URL https://arxiv.org/pdf/1103.0556.pdf. [Cited on pages 6 and 7.]

G. Zajtseva. Analysis of a 30-year series of photoelectric observations of RY Tauri. I. Search for possible periodicities. Astrophysics, 53(2):212–226, 2010. [Cited on page 21.]

G. Zajtseva, P. Petrov, I. Ilyin, R. Duemler, and I. Tuominen. RY Tauri at High Brightness. Information Bulletin on Variable Stars, (4408), 1996. URL https://konkoly.hu/pub/ibvs/4401/4408.pdf. [Cited on page 21.]

C. Zanni and J. Ferreira. MHD simulations of accretion onto a dipolar magnetosphere: II. Magnetospheric ejections and stellar spin-down. Astronomy & Astrophysics, 550 (A99), 2012. URL https://www.aanda.org/articles/aa/pdf/2013/02/aa20168-12.pdf. [Cited on pages xiii, 14, and 15.]